

Optimization of Coupled Computational Modeling and Experimentation for Metallic Systems:

Systematic Microstructural Feature – Mechanical Property Correlation for Cold-Sprayable Powders

A Dissertation

Submitted to the Faculty

of the

Worcester Polytechnic Institute

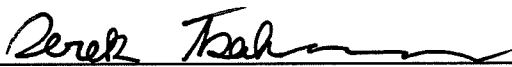
in partial fulfillment of the requirements for the

Degree of Doctor of Philosophy

in

Materials Science & Engineering

By



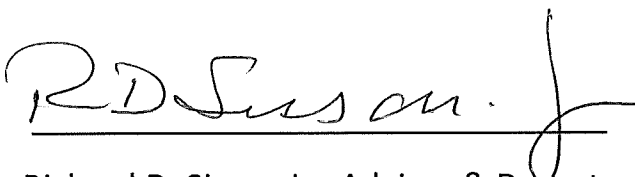
Derek Tsaknopoulos

April 2019

Approved by



Professor Danielle L. Cote, Advisor



Professor Richard D. Sisson Jr., Advisor & Department Head

**Optimization of Coupled Computational Modeling
and Experimentation for Metallic Systems:
Systematic Microstructural Feature – Mechanical Property
Correlation for Cold-Sprayable Powders**

Derek Tsaknopoulos

April 2019

1. Abstract

Additive manufacturing technologies place materials at the direct point of need of the warfighter, enabling the development of optimal, situation-specific means to produce and repair parts of Army and DoD weapons systems. In the case of solid-state AM, a full understanding of the metallic powder is critical with producing ideal consolidated material properties reliably and repeatably.

By way of iteratively coupling computational models with supportive experimental testing, one can rapidly archetype differences in processing methods, alloy compositions, and heat treatments for metallic powders that serve as feedstock for these AM technologies. Through the combination of thermodynamic models, advanced characterization, and dynamic nano-indentation, representative correlations are established between microstructural features and mechanical properties, enabling the development of enhanced feedstock materials that can achieve the specific needs of the warfighter efficiently without forfeiting quality. This represents both a holistic and a materials-by-design approach to AM through the deliberate use of computation to drive down the discovery process and allow feedstock powders to be engineered with specific properties dictated by Army requirements for performance.

In a case study of Al 6061, unique observations were made through the combination of modeling and experimentation. It was discovered that the precipitation kinetics were greatly accelerated in powders and therefore, typical heat treatment processes used for cast-aluminum alloys were not valid. Due to this shift in precipitation sequences, high-temperature treatment was limited to discourage precipitate and grain coarsening. Additionally, when compared to typical cast Al 6061, the main precipitation hardening phase shifts from Mg_2Si to $Al_4Cu_2Mg_8Si_7$, changing how aging mechanisms were accounted for. These conclusions were supported by both the computational models and experimental results. Through the generation of numerous data, the models were calibrated, enabling more efficient and precise development of tailored material characteristics from specific microstructural features to serve as an input in a holistic through-process model for a solid-state AM process and guide future experimentation.

2. Contents

1. Abstract.....	1
2. Contents.....	2
3. Introduction	3
4. Background	4
4.1. Cold Spray	4
4.2. Computational Models	4
4.3. Strengthening Mechanisms	5
4.3.1. Grain Size	5
4.3.2. Solid-Solution	6
4.3.3. Precipitation.....	6
4.4. Aluminum 6061.....	7
4.5. Through-Process Model.....	8
5. Procedure.....	10
5.1. Computational Models	11
5.2. Microscopy.....	11
5.3. Nano-Indentation.....	11
5.4. Strengthening Estimate.....	11
5.5. Iterative Feedback Loop.....	12
5.6. Through-Process Experiment: Further Testing for Feature Correlation.....	14
6. Preliminary Alloy Research	15
6.1. As-Received Results	15
6.1.1. Thermodynamic Models	15
6.1.2. Microscopy.....	18
6.1.3. Nanoindentation Hardness	19
6.2. Processed Results.....	20
6.2.1. Thermodynamic Models	20
6.2.2. Microscopy.....	21
6.2.3. Kinetic Modeling	22
6.2.4. Nano-Indentation.....	23
6.2.5. Strengthening Estimates	24

7.	Discussion.....	25
7.1.	Preliminary Analysis	25
7.2.	Relation to TPE	27
8.	Conclusion.....	28
9.	Future Work.....	29
10.	References	29
11.	Appendix A: Figures	31
11.1.	Models	31
11.1.1.	Settings.....	34
11.2.	Microscopy.....	38
11.2.1.	Scanning Electron Microscopy	38
11.2.2.	Scanning Transmission Electron Microscopy-Energy Dispersive Spectroscopy w/ Diffraction	41
11.3.	Nanoindentation.....	56
11.3.1.	As-received.....	56
11.3.2.	Solutionized.....	60

3. Introduction

The process of materials discovery and qualification has followed a consistent trend where the typical time span between material conceptualization to manufacturability is on the order of 20 to 40 years [1]. However, the pressing need for more complex components and functional materials ultimately demands quicker turnover of possible material solutions to today’s technological problems than the current approach can provide. With the rapid development of machine learning strategies and highly pedigreed data repositories, a unified procedure that couples computational materials thermodynamics and kinetics with high-throughput characterization and experimentation becomes essential.

The heuristic approach focused herein is applicable to numerous metallurgical systems and processing methods or conditions; that said, the scope of this work builds upon an ongoing metal additive manufacturing research project concerning Gas Dynamic Cold Spray at Worcester Polytechnic Institute in collaboration with the United States Army Research Laboratory. As the microstructure of the cold-sprayed consolidated material is directly dependent on the microstructure of the input powder, a full understanding of the powder’s thermo-mechanical behavior becomes key to the development of effective processes [2].

Building upon previous work performed by Danielle Belsito (Cote), Ph.D., further attention towards the Cote additive yield strength multi-variable relation was pursued to provide a justifiable and verifiable model that reliably predicts the mechanical properties of gas-atomized powders. Said model centers around inputs from thermodynamic modeling and characterization techniques, calling upon influences

from the solid solution, grain size, precipitation, and dislocation densities. [3]. While the strength model is the ultimate endpoint of this information flow, the work considered describes the interplay between the experimental and modeling subdisciplines; two distinct pillars of the modern materials community. Both approaches to solving materials design problems are generally isolated from one another. Consequently, a workable reference case with reliable success rates will enable the ability to develop situation specific cold-spray samples. At the same time, this heuristic will also be tailorable to any system where information must be gathered from the ground up and experimentally guided computation analysis is found to be the most economic option.

4. Background

4.1. Cold Spray

Cold spray is an additive manufacturing technique that produces dense, low oxide deposits by spraying powder through a de Laval nozzle at supersonic velocities. As the process is entirely solid-state, hence the “cold” spray, a number of alternative applications to thermal spray coatings are enabled, such as corrosion control and metallic repair [4]. One of the most widely known applications is the repair of magnesium rotorcraft components, using cold spray as a replacement for the technique of adhesively bonding aluminum shims over corrosion defects [5]. This process showed significant improvement of the existing method and allowed the magnesium components to be successfully reclaimed.

Several factors go into proper utilization and understanding of cold spray, including powder characteristics, particle velocity and temperature, nozzle design, and particle/substrate interaction. Powder characteristics specifically include composition, morphology, particle size distribution, and internal microstructure. To refer to this work directly, the internal microstructure of the feedstock powder is of particular interest, as any modifications made to the powder prior to being sprayed is retained in the final microstructure. As with cast metals, one of the best ways to achieve this microstructural modification is through the heat-treatment of powder, enabling better deposition rates and ultimate consolidated properties. W. Story and A. Sabard provide examples of pre-treating alloy powders, describing post-spray microstructure retention and improved particle/substrate bonding in both works [6][7]. While these works show the benefit of pre-treating the feedstock prior to cold spray, they simply compare one treatment to as-received. They do not compare various heat treatments to each other or attempt to optimize the treatments in any way.

4.2. Computational Models

As this work is being applied to complicated alloy sets with up to eight alloying elements, the types of computational models valid to the situation are limited. The CALculation of PHase Diagram (CALPHAD) employs the combination of crystallography, first principle calculations, and experimental data of simple systems to understand the inter-relationship between composition, microstructure and process conditions [8]. Thermo-Calc software was chosen as the primary computational framework due to its use of the CALPHAD process and pedigreed aluminum databases.

While general computational thermodynamics follows the minimization of Gibbs free energy, kinetics simulations involve various mechanisms depending on the complexity of the system. Thermo-Calc’s Diffusion Controlled TRAnsformations (DICTRA) utilizes seven different models, including Single-Phase, Moving Boundary, Diffusion in Dispersed Systems, Effective Diffusion, Cell, Coarsening, and Cooperative Growth [9].

The single-phase model is solved by applying a numerical procedure based on the Galerkin method for space discretization and Gaussian elimination technique with incomplete factorization to solve a system of coupled parabolic partial differential equations. The moving boundary model applies to situations where diffusion causes phase transformations, considered as two single-phase regions separated by a plane boundary and boundary migration is determined by interface diffusion. The model for diffusion in dispersed systems is suited for long-range diffusion applications, where dispersed phases act as sources of solute atoms for a continuous matrix phase. The effective diffusion model considers materials that have multiple matrix phases, dividing the multi-phase alloy into smaller volume elements that are statistically homogenous, allowing for a modified rule of mixtures. As the previously described models involve a singular calculation “cell,” the cell model considers the interconnection of two or more such cells under the assumption of diffusional equilibrium between the cell boundaries. The coarsening model applies to Ostwald ripening, assuming particle size distribution obeys the Lifshitz-Slyozov-Wagner distribution to calculate the maximum size of a single particle at the center of a spherical cell. Finally, the cooperative growth model is employed to handle mixed boundary and volume diffusion control for the concurrent growth of different phases by applying effective diffusion coefficients and assuming local equilibria [9].

Thermo-Calc’s PRISMA precipitation module extends the functionality of the thermodynamic and DICTRA models by employing Langer-Schwartz theory and Kampmann-Wagner numerical method for concurrent nucleation, growth, dissolution, and coarsening of multiple phases [3]. Generated data include temporal particle size distribution, particle number density and size, precipitate volume fraction and composition, coarsening and nucleation rates, and interfacial energy estimations.

4.3. Strengthening Mechanisms

While the computational models described above allow for the microstructural prediction of various compositions and heat treatments, they do not directly describe how those microstructures will affect the material as a whole. Consequently, various strengthening equations were used to directly correlate the data derived from the computational models to the performed nanoindentation experimentation, as yield strength and hardness are mechanically related.

For the purposes of estimating the mechanical properties of metallic systems, contributions from grain size, the solid solution, and precipitation effects are considered. By combining the nanoindentation and thermodynamic data, specific correlations between individual mechanisms and mechanical properties can be inferred.

4.3.1. Grain Size

The refinement of grain size in a metallic system has historically shown dramatic increases in strength. The magnitude of this contribution has often been quantified using the Hall-Petch equation, seen in Equation 1.

Equation 1: Hall-Petch Equation

$$\sigma_y = k\lambda^{-1/2}$$

where σ_y is the yield strength increment increase [MPa], k is the Hall-Petch coefficient [MPa*m^{-1/2}] and λ is the grain size [m].

Several studies over the years have shown the applicability of this equation; however, dislocation theory has also expanded to modify how grain size strengthening is considered. The work by Z.C. Cordero summarizes the variations of the Hall-Petch equation very well, going into the physics behind each theory [10]. Originally, Hall and Petch considered grain boundaries obstacles to dislocation motion that would eventually emit into adjacent grains when the dislocation pile-up reached a certain point. Examples of newer iterations include the activation of Frank-Read sources for new dislocations in adjacent grains and that strengthening arises directly from the work required to eject dislocations from grain boundaries. As we are looking for a general relationship between grain size and strengthening contribution, the original Hall-Petch relation was used. Future studies will explore the use of other theories and their corresponding equations. To estimate the effect of grain size strengthening, the input grain size was based on past work performed by Cote which approximated the grain size as a function of powder diameter using solidification dynamics [3].

4.3.2. Solid-Solution

Substitutional Solution Hardening by R.L. Fleischer detailed the prediction of elastic interactions that directly compute into hardness measurements [11]. The paper focused on the strengthening caused by substitution solution elements, the primary solid solution type for most commercial alloys.

As stated by Fleischer, in face-centered cubic metals, certain elastic interactions between dislocations and solute impurities accounted for the majority of solution hardening. He stated that this hardening was caused by the interactions generated by both size and rigidity differences between the solutes and the surrounding matrix, addressing the work done by Mott and Nabarro for their misfit research, as well as Crussard for his rigidity effect analysis. In Fleischer's previous 1961 paper, he calculated the elastic interaction of screw and edge dislocations via the modulus effect [12]. Using that research, Fleischer focused on the determination of the screw dislocation-size effect that, when combined with the Mott and Nabarro edge dislocation-size theory, allowed effects for both edge and screw dislocations to be fully estimated and compared. This research would eventually culminate into Fleischer's equation as seen in Equation 2.

Equation 2: Fleischer's Equation

$$\sigma_y = M \frac{G \varepsilon_s^{3/2} c^{1/2}}{700}$$

where σ_y is the shear yield strength increment increase [MPa], M is the Taylor Factor (3.06 for fcc crystals), G is shear modulus of the matrix [MPa], c is solute concentration, and ε_s is the sum mismatch term.

While solution strengthening has been further developed over the years, newer iterations involve system specific variables that would not be widely applicable to the alloys in question. For this reason, the original Fleischer's equation was chosen due to its simplicity.

4.3.3. Precipitation

Precipitation strengthening involves the interactions between dislocations and secondary phases within an alloy. As dislocations are a prime carrier of plasticity, materials will harden as the dislocation motion is impeded by the secondary phases. This hardening can occur through several different methods but can be simplified into two separate categories, cutting and bowing.

Cutting involves the variety of interactions as a dislocation shears through a deformable precipitate. Coherency strengthening occurs when a deformable precipitate has a coherent interface with the matrix, causing strain fields on the surrounding matrix. Modulus strengthening occurs from dislocation energy changes due to the varying shear modulus between a deformable precipitate and the matrix. Chemical strengthening occurs from the interaction between surface energy of the deformable precipitate-matrix interface and the dislocation. Order strengthening is also a factor to precipitation cutting calculations but is not relevant to the systems considered.

Precipitation bowing occurs when a precipitate is strong enough to resist dislocation shearing. As a result, dislocations will bow around the precipitate instead, a mechanism described by the Orowan equation [13]. For precipitates that are not inherently too “strong” for dislocation shearing, a critical radius will occur where the mechanism for dislocation passage switches between cutting and bowing as the precipitate grows larger. As dislocations will always choose the path of least resistance, this point refers directly to the energy required for a dislocation to pass a precipitate.

While both cutting and looping were considered for the powder alloys, looping was chosen as the primary strengthening mechanic as the precipitates very rapidly left the cutting regime. These contributions were quantified using a modified Orowan Looping equation seen in Equation 3.

Equation 3: Modified Orowan Looping Equation [14]

$$\sigma_{Orowan} = M \frac{0.4Gb}{\pi\sqrt{1-\nu}} \frac{\ln\left(\frac{2\bar{r}}{b}\right)}{\lambda_p}$$

where σ_{Orowan} is the shear yield strength increment increase [MPa], M is the Taylor Factor (3.06 for fcc crystals), G is shear modulus of the matrix [MPa], b is the burgers vector of the matrix [m], ν is the Poisson ratio of the matrix, \bar{r} is the mean radius of the circular cross-section of a random plane for a spherical precipitate ($\bar{r} = \sqrt{\frac{2}{3}}r$)[m], and λ_p is the precipitate interparticle spacing [m].

4.4. Aluminum 6061

Conventional Al 6061 is a heat-treatable aluminum alloy with primary strengthening from β -Mg₂Si and its corresponding metastable phases. These phases transition from needles (β'') to rods (β'), and from rods to equilibrium plates or cubes (β) during thermal treatment. Typical heat treatments aim to create a homogenous microstructure via an initial solutionization step. Solutionization is followed by a rapid quench to retain the metastable microstructure and concluded with an aging step to precipitate varying amounts of β' and β'' as required per ones' desired material performance. Additionally, 6061 contains various Fe-rich intermetallics due to the low solubility of Fe in Al, which must be accounted for, since the Fe species are difficult to dissolve during solutionization due to their high melting temperatures [15]. A typical aging curve for cast 6061 after solutionization can be found in Figure 1. Observing the 171°C line, precipitation strengthening for this dataset resulted in about a 75% increase in yield strength.

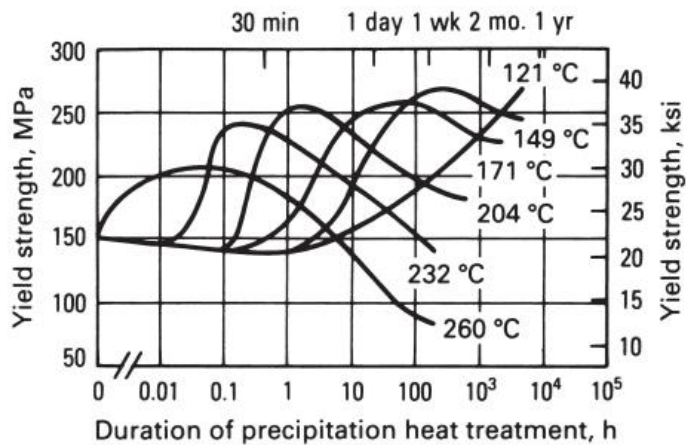


Figure 1: Typical aging curves for solution heat treated aluminum alloy 6061 [16]

4.5. Through-Process Model

This work was performed in collaboration with the Army Research Lab, where WPI partnered with several universities with the goal of developing a through-process model for Gas Dynamic Cold Spray. This model would enable the user to rapidly prototype multiple different conditions, ranging from gas atomization to the final consolidated mechanical properties. WPI was assigned the understanding of the feedstock powder, focusing on both powder production and powder processing. As such, our model would be able to track differences in microchemistry, microstructure, process parameters, degassing, heat treating, blending, and milling, which would then culminate into a predictive mechanical property model for the powder itself. This model would then feed into other models that involved the cold spray directly, allowing for continuous simulation of the overall process. An outline of this system can be seen in Figure 2.

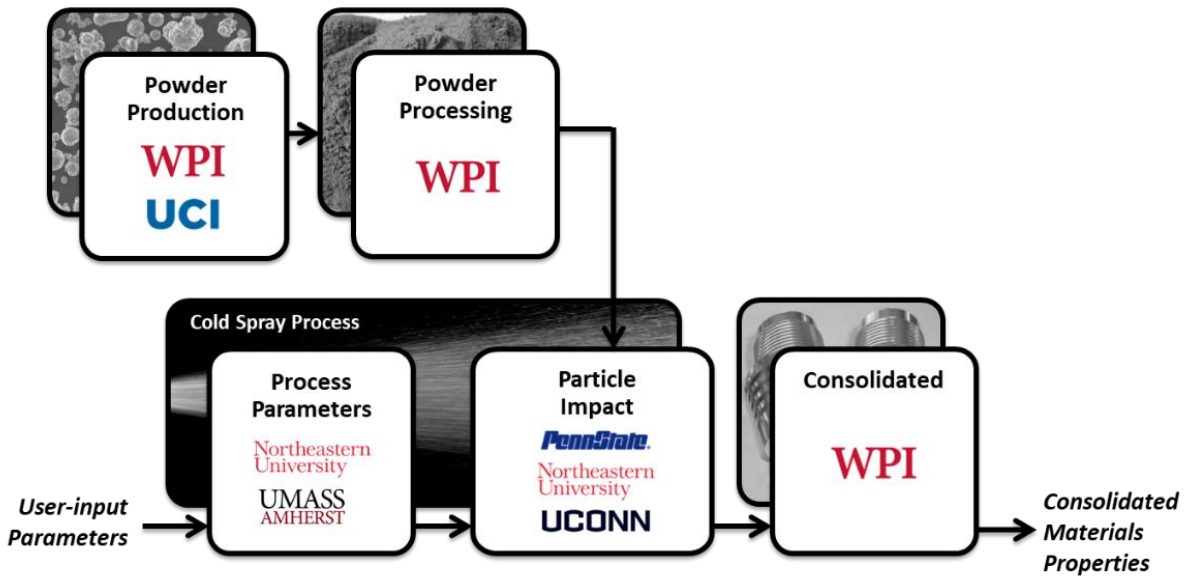


Figure 2: ARL Through-Process Model Outline

The University of California Irvine has been tasked with analyzing variables in the gas atomization process itself using their own atomization column, whereas previously we could only make inferences on the commercially purchased powder the group used. Future projects may entail the development of optimized alloys for cold spray, rather than the typically used cast aluminum alloy compositions.

The Pennsylvania State University utilized a Preston-Tonks-Wallace plasticity finite element model using ABAQUS to simulate the deformation effect of multi-particle impacts onto a substrate, taking special note of the effect the powder's microstructure had on the resulting dislocation density formation. This work was done directly with WPI, taking microstructures characterized by the WPI group and loading them directly into the model. The eventual goal of this model is to build of a multi-layer cold spray sample that accurately estimates the consolidated properties, specifically accounting for the effect dislocations have on mechanical properties[17].

One group at Northeastern University focused on the cold spray gas stream itself, optimizing parameter selection while involving losses due to particle loading into the stream. These models ultimately allow the user to estimate changes in particle impact velocity and temperature due to changes in the spray system, giving complete analysis on deposition cost and time [18]. Northeastern, in collaboration with University of Massachusetts Amherst, also pursued bilinear Johnson-Cook models to explore the effects material damage, high-strain-rate plastic flow, interfacial friction, and heat generation due to plasticity [19].

A Quasi-coarse-grained dynamics (QCGD) method was performed at University of Connecticut to model the mesoscale behavior of single particle impacts onto a substrate. These models allowed the simulation of kinetics related to pressure evolution and propagation and heat generation and dissipation for both the particle and substrates. Specific focus was put on the upward flow of metal from the particle/substrate and its role in bonding (jetting formation) [20].

Through the combination of the models from each group, an intrinsic understanding of the overall cold spray process would be enabled, allowing for any variable to be computationally changed but still understood. This would dramatically decrease the amount of trial and error needed in the cold spray process to find optimal conditions for a given situation. This is particularly important in ARL cold spray where the process is relatively expensive, and qualifications are tight. The work detailed below outlines some of the contributions WPI has made to the Through-Process Model and how future experimentation can be guided through the heuristic approach.

5. Procedure

For this work, gas-atomized powder was acquired from Valimet, Inc. (Stockton, CA, USA). The powder was subjected to compositional chemistry testing / elemental analysis, specifically, Inert Gas Fusion (IGF), by Luvak Laboratories, Inc. (Boylston, MA, USA). The received powder particles were mechanically sieved using laboratory test sieves (Humboldt Mfg. Co., Elgin, IL) compliant with ASTM E 11-17 into seven classifications to aid in the repeatability of selecting similarly sized particles for analysis. The size classifications are < 25 μm , 25-32 μm , 32-28 μm , 38-45 μm , 45-53 μm , 53-63 μm , and > 63 μm . The compositional chemistry found via IGF of gas-atomized Al 6061 powder is presented in Figure 3.

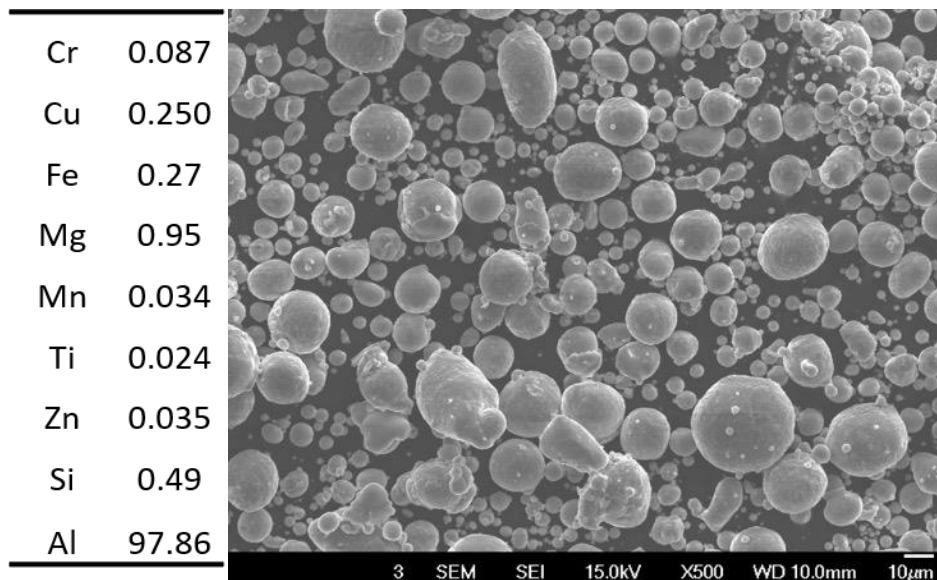


Figure 3: Valimet 6061 Composition (wt %) and SEM

When compared to the ASTM standard, this composition falls within acceptable ranges. The 38-45 μm category was considered for this present study. Using a differential scanning calorimeter (DSC) (TA Instruments, New Castle, DE, USA), samples were treated in a nitrogen environment at 530 $^{\circ}\text{C}$ for 1 hour with a heating rate of 80 $^{\circ}\text{C}/\text{min}$ for a solutionization step followed by an aging step at 170 $^{\circ}\text{C}$ with a heating rate of 10 $^{\circ}\text{C}/\text{min}$ for a given time. A cooling rate of 120 $^{\circ}\text{C}/\text{min}$ using liquid nitrogen was used for all quenching steps.

5.1. Computational Models

In order to rapidly iterate the thermodynamic and kinetic models based on calibrations from experimental results, Thermo-Calc's graphical mode was employed for its ease of use as compared to console mode. The composition found via IGF was used in the System Definer using the TCAL6 and MOBAL5 databases using the 2019-A edition, seen in Figure 21. From the System Definer, the Equilibrium Calculator was used to establish the equilibrium microstructure between 100°C and 700°C, seen in Figure 22. Also from the System Definer, the Scheil Calculator was run using the settings described in Figure 23. The Precipitation Calculator was used both at 530°C and 170°C to simulate solutionized and aging respectively. Grain boundary precipitation was assumed, and the grain size was changed to 2E-6 meters to match previous characterization work. An Isothermal calculation type was also used to simplify the calculation time as there were no evident differences using non-isothermal heating and cooling inputs from the DSC procedure. Future work will explore variation in heating and cooling rates using the non-isothermal calculation type. As these databases were built using data from both castings and wrought samples, minor adjustments were made to the nucleation site parameters to accelerate the timeline of nucleation and growth to make the databases more readily applicable to powder systems. This adjustment can be seen in Figure 24 under Mobility enhancement prefactor.

5.2. Microscopy

Samples were prepared for TEM analysis using a gallium focused ion beam (FIB) (Helios 660 Nanolab, ThermoFisher Scientific, Waltham, MA, USA) on a molybdenum Omni-grid. These samples were then characterized using a probe-corrected TEM (Titan Themis with ChemiSTEM, ThermoFisher Scientific, Waltham, MA, USA) and energy dispersive X-Ray spectroscopy (EDS) (Super-X, ThermoFisher Scientific, Waltham, MA, USA) with an accelerating voltage of 300 kV.

5.3. Nano-Indentation

Dynamic nanoindentation testing was performed as described by the Oliver-Pharr analysis and the newly acquired iMicro Pro nanoindentation system manufactured by Nanomechanics, Inc. (a KLA-Tecnor company, Oak Ridge, TN, USA). The InForce 50 mN actuator, equipped with a Berkovich diamond indenter tip that had an initial rounding endpoint radius of 86 nm, was used in indenting the polished cross sections of Al powder particles. In contrast with the limited nature of the Keysight G200 Nano indenter's static indentation capabilities, the iMicro Pro enables the elastic, elastic-plastic, and fully plastic transitions to be captured.

5.4. Strengthening Estimate

The strengthening mechanisms were used as a reference for the significance determination for certain microstructural features. Future work will calibrate these estimations to provide predictions that are directly comparable to literature results. Solid solution strengthening utilized element specific data in combination with Fleischer's equation. The matrix composition was determined through both modeling and characterization analysis. Grain size strengthening used a Hall-Petch relationship as a function of a grain size-powder size relationship developed by Cote [3]. As only the 38-45 μm sieved powder was used within the scope of this work, an average size of 40 μm was used for calculations. Precipitation strengthening utilized kinetic data obtained directly from Thermo-Calc simulations, calibrated in accordance with the findings from the characterization performed by the cold spray ARL project team.

Dislocation strengthening continues to be developed in collaboration with Dr. Jeremy Schreiber of The Pennsylvania State University's Applied Research Lab. At present, the dislocation strengthening effect is considered negligible for feedstock powder calculations.

5.5. Iterative Feedback Loop

In order to build a fundamental understanding of a metallic alloy, the process of iteratively combining modeling and experimentation can be found in Figure 4, dubbed the Iterative Experimental Model. This flowchart outlines the thought process, focusing on heat treatment effects considered herein, and the rest of this work will be arranged in a manner matching it. The overall goal of this process is to be able to accurately track the effect a particular microstructural feature has on the mechanical properties of the system, while also enabling the user to know how to best take advantage of this knowledge. An example of this would be knowing how a specific precipitate provides the best strength contribution and thus giving recommendations on how to maximize its growth, whether it be from heat treatment or microchemistry adjustments.

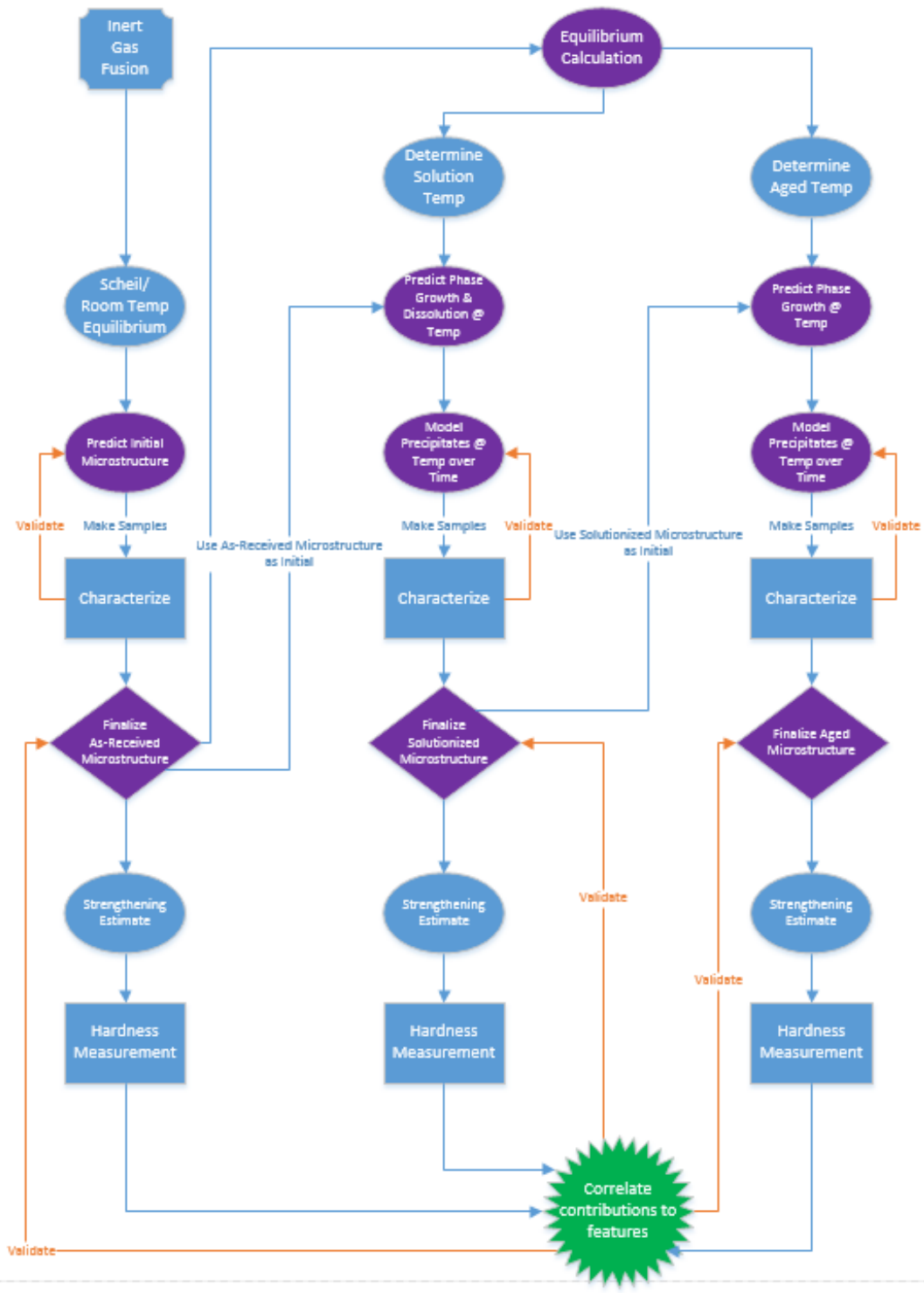


Figure 4: Iterative Experimental Model

5.6. Through-Process Experiment: Further Testing for Feature Correlation

While the Iterative Experimental Model enables WPI to contribute to the Through-Process Model (detailed later), much work still needs to be done by each group before computational modeling can fully replace any portion of experimental testing for the cold spray process. This is because each of these models must be calibrated through careful experimentation systematically comparing individual variables to see their effect on the final microstructure. Specifically, in context of the Iterative Experimental Model, the effects of heat treatment on the final consolidated properties have not been fully explored for any alloy system. While heat treatments have been studied and varied, only inferences have been able to be made, without fully understanding why something is working or not working. As a result, it has been difficult to give recommendations of heat treatments for any system as there is not a detailed guideline of what to look for in a consolidated material. This is a detriment for both future experimental testing and every type of computational model used at present. Consequently, the Iterative Experimental Model was utilized to serve as a precursor to a fleshed-out experimental project with ARL involving every project team, dubbed the Through-Process Experiment seen in Figure 5.

The goal of this project is to serve as a basis for the calibration of the Through-Process Model, where the significance of specific adjustments to microstructure, in this case being heat treatment, are explored for every aspect of cold spray. With every group collaborating directly on the same sets of powder, direct correlations can be made between microstructural features, mechanical properties of both the powder and final consolidated material, and optimized cold-spray characteristics. The first of these Through-Process Experiments is to involve the variation of heat treatment for Al 6061, but the overall process will eventually expand to other metallic systems and other parameter variations. This will ultimately allow for a calibrated Through-Process Model with pedigreed data that can accurately predict situations not included within the Through-Process Experiments.

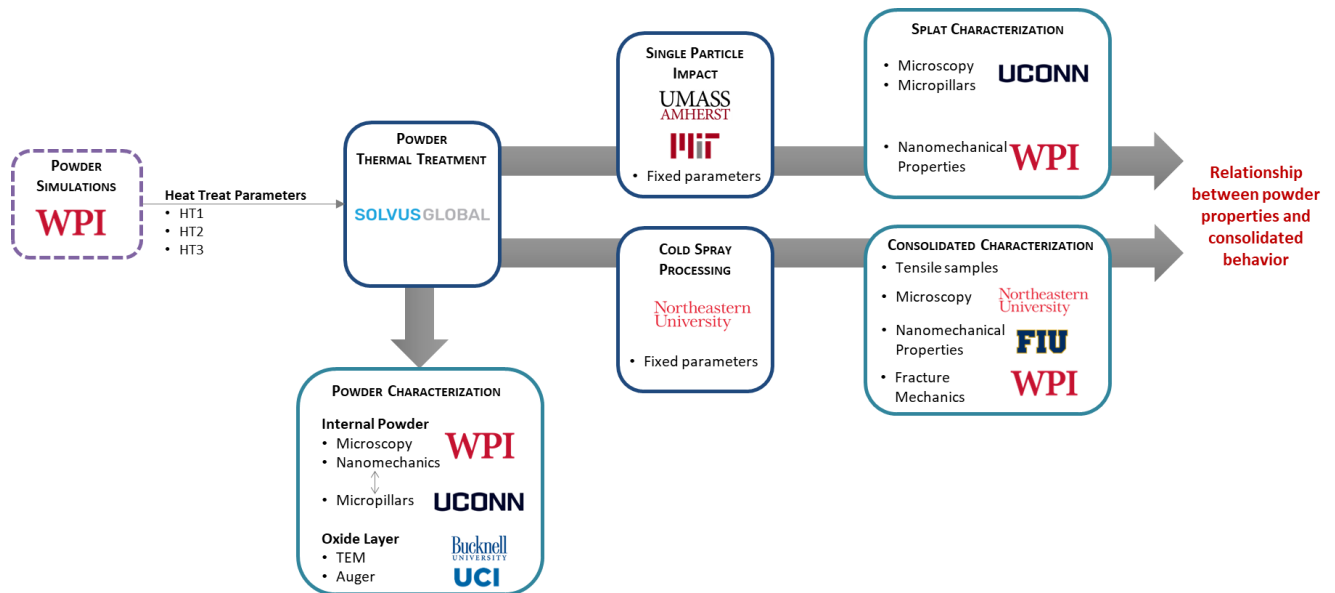


Figure 5: ARL Future Project: Through-Process Experiment

After choosing multiple treatments of interest using the Iterative Experimental Model, the powder will be processed in a fluidized bed to provide consistent and reliable treatments and bagged in an inert environment to minimize environmental effects on the longevity of the powders. University of California Irvine and Bucknell University will both characterize the oxide layer of the feedstock powder, to analyze the effect of the treatments themselves as well as comparing them to past work that was not inertly packaged. University of Connecticut will perform micropillar compression testing to provide a comparison point for the bulk nanoindentation results that WPI will perform. This data will also later be compared to compression pillars formed from individually splatted particles to directly analyze dislocation density effects [21].

Single particle impact will be performed by both University of Massachusetts Amherst and Massachusetts Institute of Technology, using laser-induced ablation of thin gold foils [19][22]. This data will allow the direct measurement of critical impact velocity, allowing for the effect of certain features to be observed without the variability of the entire cold spray process. This will also provide splat samples for further characterization by University of Connecticut and WPI.

Most of the powder will go to Northeastern University, who will do the spraying for each treatment set. A small portion of these samples will be kept as as-sprayed bars to study the bonding interface, the rest will be machined into tensile samples. The spray parameters for these bars will be optimized based on previously spray knowledge of 6061 but kept consistent between the different treatment sets so not to add extra variables. These bars will be studied by a combination of Northeastern, WPI, and Florida International University in order to observe post-spray microstructural features, nanomechanical comparisons [23], and fracture mechanics.

The overall goal of this project is to not only answer specific questions regarding the optimization of colds-sprayed Al 6061, to be specified later, but also create an efficient framework for multi-university collaboration to work cohesively rather than adjacently.

6. Preliminary Alloy Research

To obtain an intrinsic understanding of the Al 6061 system, the Iterative Experimental Model was employed. The experimental research was assisted by the entire Cote research group. This knowledge was used both in WPI's portion of the Through-Process Model and in guiding the Through-Process Experiment initial treatment conditions.

6.1. As-Received Results

After obtaining the chemical compositions found in Figure 3, the first steps in predicting the effect of thermal treatment on Al 6061 was to establish a baseline microstructure for the as-received powder. Strengthening contribution equations were not applied to the as-received powder as many of the equations are more applicable to equiaxed microstructures with discrete phases.

6.1.1. Thermodynamic Models

Given that gas-atomization is a non-equilibrium solidification technique, the Thermo-Calc Scheil calculation was used to estimate the initial microstructure of the alloy. The Gulliver-Scheil equation used in the calculation is highly representative of gas-atomization as it becomes more accurate the faster the cooling rate and gas-atomization cooling rates are on the scale of 1×10^4 to 1×10^5 °C/s. A main feature of this equation is that it assumes no diffusion in the solid and infinite diffusion in the liquid. As seen in

Figure 6, Thermo-Calc predicts several different phases would form during solidification, with the two most prominent phases being Mg_2Si and $Al_{13}Fe_4$. This directly contested the CCT work performed by Cote, who contested that no Mg_2Si would form during solidification [3].

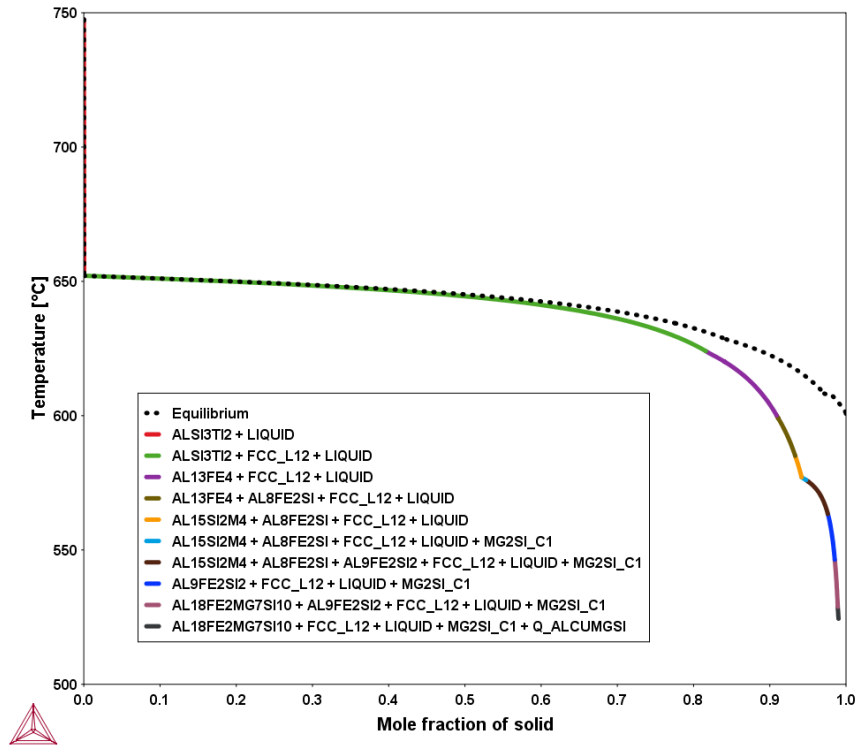


Figure 6: Thermo-Calc Gulliver-Scheil Diagram for Al 6061

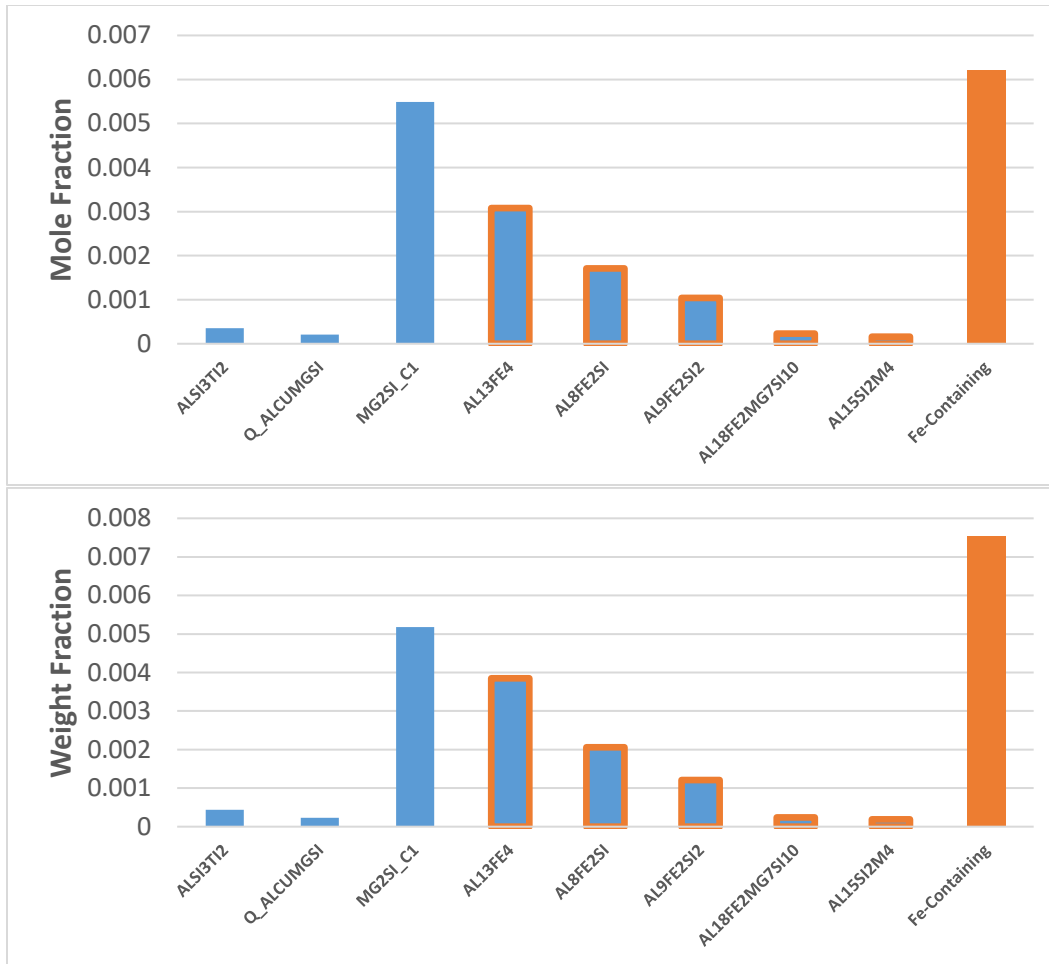


Figure 7: Representations of amounts of precipitates formed during solidification via Thermo-Calc Gulliver-Scheil model. Heavy Metal-containing precipitates outlined and totaled in orange

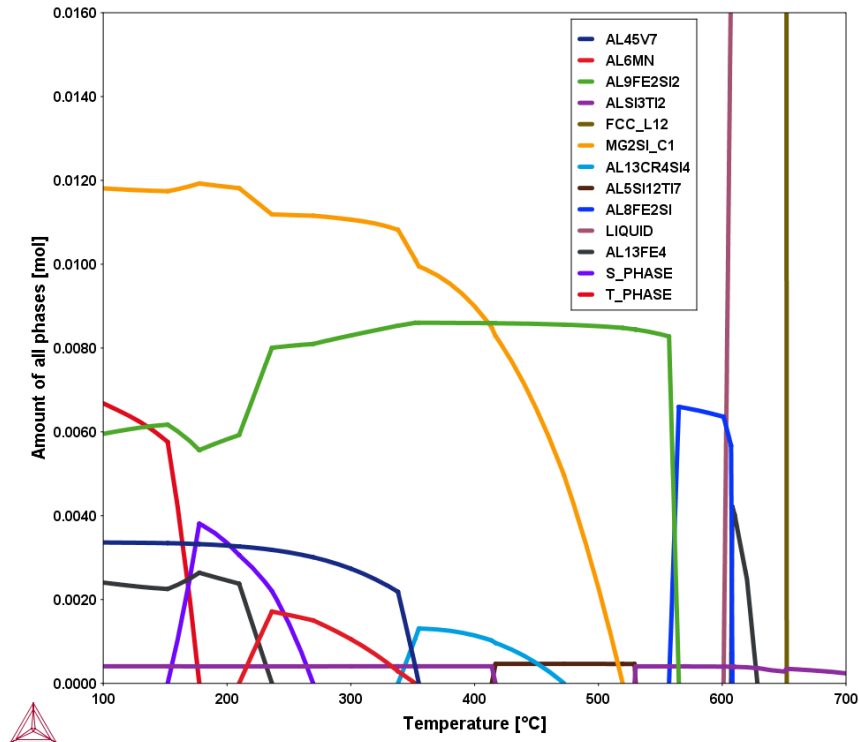


Figure 8: Thermo-Calc Equilibrium Diagram for as-received Al 6061

The equilibrium diagram found in Figure 8 shows the expected Al 6061 precipitate stability at equilibrium, with Mg_2Si , Al_6Mn , and $Al_9Fe_2Si_2$ being the most prominent at low temperatures. In the case of 6061 casting, the actual precipitate formation of a sample can be found somewhere between the two diagrams, where the assumptions of the Gulliver-Scheil calculations are not applicable and additional nucleation and growth would occur during cooling and at room temperature. In the case of this work, it was initially assumed that the Scheil model would be perfectly applicable to powders. The applicability of this assumption and its consequence for aluminum powders was tested experimentally with a combination of metallography characterization methods for various treatment conditions.

6.1.2. Microscopy

The microstructure of the as-received powder was focused upon by Cote group members Kyle Tsaknopoulos and Caitlin Walde [15]. To summarize the conclusion of their work, the precipitates of the as-received powder was found to form a network-like structure only along the grain boundaries with nearly no bulk nucleation. An example of structure can also be seen in previous work done by Ballie McNally (Haddad), displayed in Figure 30. When performing phase analysis of these networks, it was determined to be two individual phases. The dark spots corresponded to Mg_2Si and the light phases corresponded to $Al_{13}Fe_4$, which has strong agreement with the conclusions made in the previous section (Figure 7). No other phases were able to be identified, possibly due to a lack of nucleation or that simply they were not visible within the Mg_2Si - $Al_{13}Fe_4$ network. As the thermodynamic models do not provide an accurate representation of mean radius or volume fraction of these precipitates, the data obtained by Tsaknopoulos and Walde was used as the initial precipitate microstructure for the later solutionized step. Addressing the Through-Process Experimental Mode, the finalized as-received microstructure was

obtained, allowing for us to progress to the feature correlation step as well as bridging off to the thermal treatment step.

6.1.3. Nanoindentation Hardness

Nanoindentation arrays on multiple powder particles were carried out to find the hardness and elastic modulus, at a given depth, of the as-received powder. As a result, the hardness was determined to be 1.224 GPa and the elastic modulus that of 68.61 GPa. An example of the Oliver-Pharr extracted hardness vs depth curves, which is a form of analytically discerning essential indentation responses from applied load vs. indentation depth data, from the iMicro Pro can be found in Figure 9.

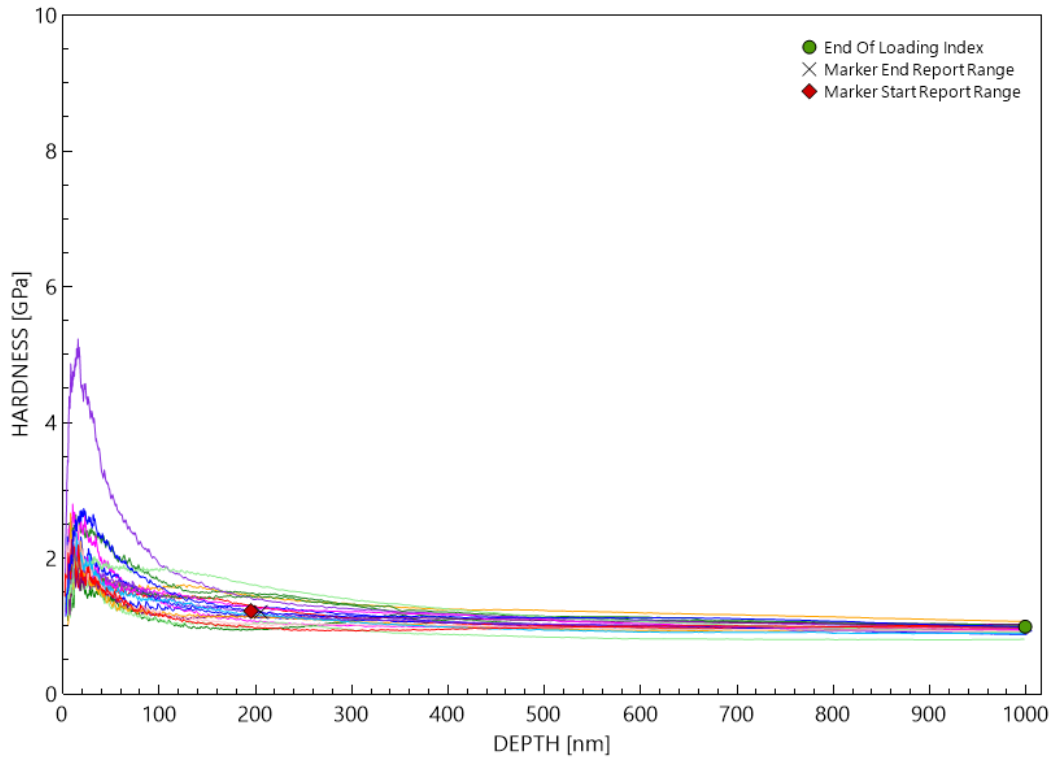


Figure 9: Hardness vs Depth data for AR-6061

Using this data, a depth of 200 nm was chosen as the point of reference for reporting the standardized properties of hardness and elastic modulus. This depth was chosen to account for the work-hardening that occurred upon indentation, which is shown to peak around 20 nm on the above figure, while avoiding the influence from the relatively less stiff compression mounting material at greater depths. Furthermore, fully plastic contact is thought to be achieved by 200 nm from the indented samples as well. The significance of these properties will be discussed alongside the properties of the treated samples found in the Processed Results section.

6.2. Processed Results

As seen in the Iterative Experimental Model, the as-received microstructure described in Section 5.1 was used to determine the effect of thermal treatment upon the microstructure and mechanical properties.

6.2.1. Thermodynamic Models

The first step to properly determine what was going on in these systems is to look again at the equilibrium data. Using literature as a basis, a conventional T6 treatment for 6061 is a solutionization step at 530°C and an aging step at 170°C. To analyze the applicability of the solutionization temperature, a zoomed in version of the Figure 8 can be found in Figure 10. Based on this diagram, one can make several conclusions. This solution treatment should not result in incipient melting based on the liquid phase stability at roughly 600°C. Mg₂Si should be mostly put into solution but some of the more coarsened particles might remain. Finally, the intermetallic Al₉Fe₂Si₂ is stable up to 560°C; therefore, it will be impossible to solutionize our microstructure completely and coarsening must be watched for. When coupling this conclusion with the work found in Section 5, it was concluded that the transformation between Al₁₃Fe₄ to Al₉Fe₂Si₂ would occur. The aging temperature agrees with the highest low-temp phase found on Figure 8, working to maximum the precipitation of Mg₂Si. This temperature also achieves a secondary goal of maintaining the stability of Al₉Fe₂Si₂, whereas a lower temperature would possibly result in the formation of Al₆Mn.

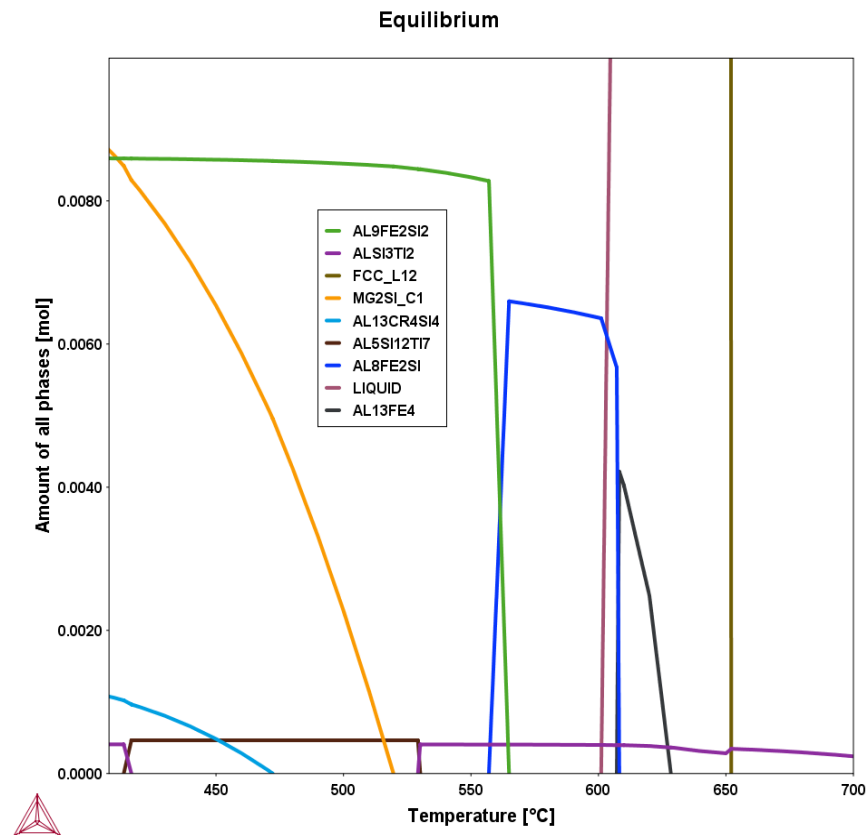


Figure 10: Zoomed Thermo-Calc Equilibrium Diagram for Al 6061

As the initial microstructure of powders are very different than their casting/wrought counterparts, the thermodynamics and kinetics cannot be assumed to be consistent between systems. Nevertheless, the

conclusions made from these equilibrium diagrams provides insight into the types of structures that were looked for during microscopical characterization. The main goals of the characterization were the confirmation of determined phases and the time scale for their dissolution, transformation, nucleation, or growth.

6.2.2. Microscopy

In the case of 6061, past work by Caitlin Walde concluded that a dissolution time of 1 hour at 530°C was most appropriate. It was discovered to be extremely difficult to remove some of the larger Mg_2Si precipitates, with only small reductions in volume fraction after 1 hour [24]. On the other hand, significant increases in the size of iron precipitates occurred the longer the powders were held at temperature. As coarsened iron particles are generally considered to be nucleation sites of fracture, 1 hour was chosen to balance the reduction in Mg_2Si without overly coarsening the iron precipitates. These conclusions were made using simply SEM characterization, only being able to differentiate the dark Mg_2Si and the light iron-containing precipitates from the surround matrix, prior to identifying the initial iron phase as $Al_{13}Fe_4$ in the as-received condition.

Using the solution temperature and time of 530°C for 1 hour, more in-depth characterization was performed to confirm the microstructure of the solutionized powder. The conclusion of this work was that the smaller Mg_2Si particles were completely removed while the larger ones spheroidized from the network-like structure found in the as-received condition [15]. Simultaneously, it was confirmed that the as-received $Al_{13}Fe_4$ phase completely transformed to $Al_9Fe_2Si_2$, with no remaining $Al_{13}Fe_4$ or other iron phases nucleating. The newly formed $Al_9Fe_2Si_2$ can also be found along the grain boundaries. This matches very well with the conclusions discussed in Section 6.2.1 and the size and volume fraction information will be used later in Section 6.2.3 to calibrate the kinetic portion of the models. It was also observed that chromium and manganese segregated to the iron-containing precipitates, observed in Section 11.2.2.2. As these maps are based upon weight percent, the true influence of these elements is misrepresented. Measurements of atom percent of these precipitates performed by Tsaknopoulos and Walde showed that the actual contributions were only a couple percent overall, implying that the Cr,Mn-containing phases are naturally aged heterogeneously upon the preexisting $Al_9Fe_2Si_2$.

After determining the appropriate solutionization step, samples were aged at 170°C for various time increments. In order to track the growth of the aging precipitates, samples were made at 2, 4, 6, 8, 10, and 25 hour increments, all of which were solutionized first. Special attention was given to the 8 and 25 hour samples to display the conventional T6 aged microstructure (Figure 36 and Figure 37) and a representative “equilibrium” microstructure (Figure 41 and Figure 42) respectively. In the Low-Mag STEM-EDS maps, one can see that the coarsening Mg_2Si and $Al_9Fe_2Si_2$ precipitates are roughly the same size as those in the solutionized samples, confirming that the coarsening kinetics are not noticeable at these temperatures. When looking at the High-Mag maps however, a very different microstructure as to what was predicted is seen. In both treatments, a series of cross-hatched precipitates can be found along every grain boundary and in some bulk locations in the case of the 25 hour. While these phases were initially thought to be β'' or β' , which would agree with the previous modeling and literature review discussed, STEM-EDS of the specific precipitates (Table 2 and Table 4) confirmed the presence of copper, which would not be present in Mg_2Si or its metastable forms. For additional validation, the lattice parameters of these precipitates were measured to be 0.26 and 0.214 using both diffraction patterns and the direct measurement of the lattice fringes in the HRTEM images. Coupling both the

atomistic composition with the lattice parameter, this phase was identified as Hexagonal $\text{Al}_4\text{Cu}_2\text{Mg}_8\text{Si}_7$, commonly known as Q-AlCuMgSi. An important note is that this phase was already in its equilibrium state at 8 hours aging, which would normally correspond to the maximum fraction of β'' in typical Al 6061. Based on these results, it was concluded that both the thermodynamics and kinetics of the powders would need to be modified to account for these changes in aging behavior.

6.2.3. Kinetic Modeling

In order to understand why Q-AlCuMgSi formed, additional simulations were ran to try to understand what was going on. Using the information obtained in the as-received and solutionized microscopy, the 530°C treatment was simulated, focusing on the dissolution of Mg_2Si and the transformation of $\text{Al}_{13}\text{Fe}_4$ to $\text{Al}_9\text{Fe}_2\text{Si}_2$ (Figure 15, Figure 16, Figure 17). These models were calibrated using characterization performed by the Cote group. It was assumed that the complete dissolution of Mg_2Si was not possible based on this previously run characterization, believed to be due to the increased stability within the fine-grain structure. A minor adjustment of 1400 joules/mole was added to the Mg_2Si phase stability to simulate this, resulting in the plateauing effect seen in Figure 17. This adjustment can be seen in Figure 25.

An assumption was then made that the iron-containing precipitates would not have the kinetics necessary to change at the aging temperature of 170°C. As a result, the heavy-metal phases that formed during the solutionization treatment were assumed constant, contributing elements were removed from the system, and the matrix composition was modified. With these elements being removed from the system, the simulation was simplified to include only the remaining elements that would react at the low temperatures (Mg, Cu, Si) using the data derived from the solutionization model. The equilibrium model showing this modification can be found in Figure 11 on the left. However, as there is still Mg_2Si remaining after solutionization, it was theorized that there would not be additional Mg_2Si nucleation due to a lower driving force from the local equilibrium. To simulate what would happen in that case, Mg_2Si was removed as a possible precipitate, resulting in the right figure. As a result, Q-AlCuMgSi becomes the primary precipitate to form, matching our experimental results.

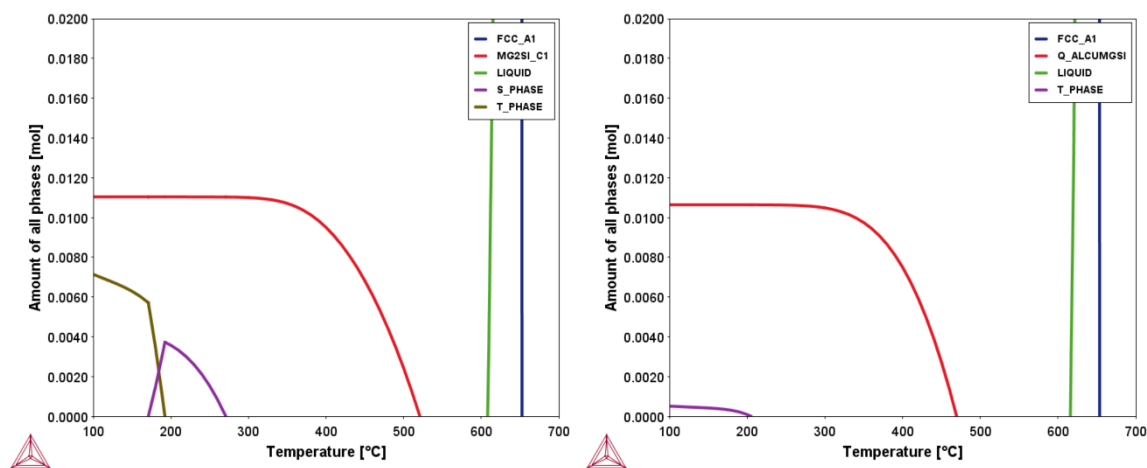


Figure 11: Thermo-Calc Equilibrium Diagram for modified post-solution Al 6061 with Mg_2Si removed on right diagram

Using the matrix composition obtained in the above described model, a new simulation was ran to display the growth of the Q-AlCuMgSi (Figure 18, Figure 19, Figure 20). This simulation also included Mg₂Si with the initial size and volume fraction of the post-solution simulation, in order to confirm that there would not be any additional Mg₂Si nucleation due to the precipitates already in the system. The simulation was further calibrated using the mean radius and volume fraction estimated from the STEM-EDS for the 8 and 25 hour samples (Figure 37 and Figure 42). It was however discovered that data pertaining to Q-AlCuMgSi in the Thermo-Calc database for coarsening is currently inadequate under 280°C, so direct correlations cannot be made at this time. The models were still ran and compiled in preparation of modifications to the database itself while still allowing microstructural correlations to be made in the meantime.

6.2.4. Nano-Indentation

Using the same nanoindentation techniques previously discussed, the hardness and modulus for the treated 6061 samples are summarized in Table 1. General observations include a peak hardness at 6 hours with a decrease in hardness by 8 hours the plateaus to at least 10 hours. This hardening was assumed to be attributed to the precipitation and growth of the Q-AlCuMgSi with the eventual softening when the precipitate reached its overaged condition. This assumption was also verified using the combination of the Thermo-Calc data obtained with the strengthening mechanisms described in Section 5.4, balancing the contributions to strengthening from Q-AlCuMgSi and solution strengthening. Another notable feature was that modulus for the solutionized sample was higher than that of the 10-hour sample, despite have relatively the same hardness. This agrees with the general concept that the over-coarsening of precipitates is detrimental to most mechanical properties (hardness, modulus, fracture toughness, etc).

Table 1: Nanoindentation outputs for Al 6061

Sample	Hardness [GPa]	Hardness SD [GPa]	Modulus [GPa]	Modulus SD [GPa]
As-Received	1.224	0.176	68.81	3.77
Solutionized	1.092	0.088	70.98	2.96
2 Hour	1.157	0.128	64.17	11.35
4 Hour	1.211	0.166	62.42	6.34
6 Hour	1.387	0.156	63.87	5.29
8 Hour	1.126	0.164	64.02	5.66
10 Hour	1.108	0.133	65.34	2.98

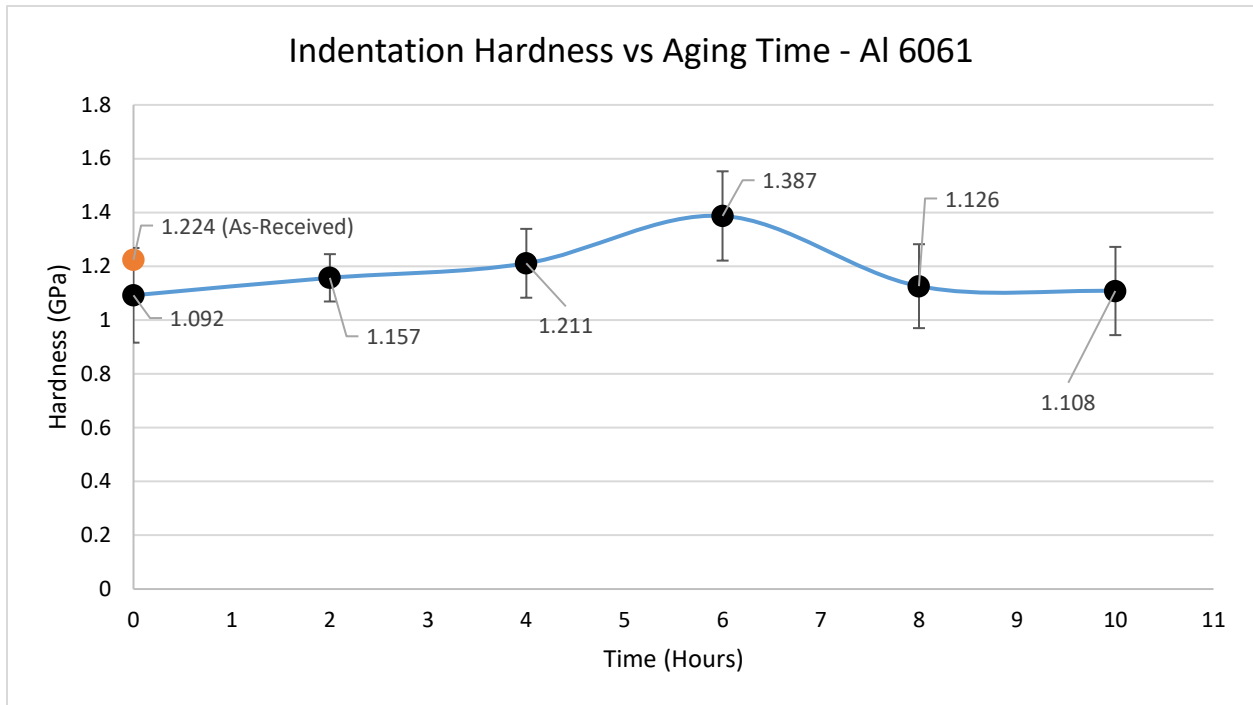


Figure 12: Indentation Hardness for aged 6061 at 170°C. Samples solutionized at 530°C for 1 hour

6.2.5. Strengthening Estimates

Numerous assumptions were made based on the characterization work performed by the Cote group to reduce the variability of certain contributions within strengthening correlations. It was assumed that:

- The grain size was constant within the range between solutionization and final aging.
- The matrix was completely homogenized without any segregation.
- The mean radius and volume fraction of the precipitates, Mg_2Si and $Al_9Fe_2Si_2$, remained constant after solutionization, supported by the work of Tsaknopoulos-Walde.
- The only precipitate to form during aging was Q-AlCuMgSi.
- All precipitation strengthening will be via Orowan Looping due to the size and coherency of the Q-AlCuMgSi precipitates.
- After solutionization and aging, dislocation strengthening is negligible.

Using these assumptions coupled with the equations found in Section 4.3, the comparative magnitudes of each contributions were inferred for feature correlation. Solid solution strengthening was a major initial strengthening source, which eventually decreased as the matrix is depleted from precipitate coarsening. Grain size strengthening also had major contributions, to be expected in powder metallurgy. Precipitation strengthening also contributed significantly but could easily over coarsen at high temperatures. Q-AlCuMgSi was found to grow until silicon was completely depleted from the matrix, which was verified by both Figure 18 and Table 3 . At this point the precipitate would begin to coarsen as volume fraction is held constant, leading to overaging and a decrease in precipitation strengthening.

7. Discussion

7.1. Preliminary Analysis

Comparing the data displayed in Sections 6.2.4 to that of typical Al 6061, correlations were made between the specific microstructural features and the estimated/calculated hardness measurements. For these general correlations, differences between micro-indentation and nano-indentation were considered negligible and future studies will further investigate this claim. Using work by Aytekin Polat [25] as a point of reference, the contribution of grain size strengthening can be directly observed by comparing the hardness of the solutionized samples, where both matrix and precipitate conditions should be similar. Cast solutionized Al 6061 was found to have a hardness of 54 HV, where the powder was about 111.3 HV (1.224 GPa). Next, the powder peak hardness was found to be at 6 hours of treatment, attributed to the optimal size and volume fraction of Q-AlCuMgSi, where cast Al 6061 does not reach peak hardness until after 10 hours of treatment [16], [25]. Finally, the accelerated kinetics of powders can be observed at 10 hours, where the Q-AlCuMgSi has already reached its overaged condition, whereas cast 6061 will not reach maturation until over 36 hours of aging, observable back in Figure 1.

An important point of note is that for the as-received, solutionized, and aged samples, precipitates were found almost exclusively along the grain boundaries. As precipitate strengthening contributions are generally assumed only applicable to bulk nucleation, it is possible that these secondary phases would not contribute to the strength of the alloy other than the depletion of solid solution strengthening. On the other hand, clear differences can be seen in Figure 12 between the different conditions which directly match expected results based on strengthening estimations. As a result, it is theorized that the precipitates along grain boundaries will still contribute on the overall strength of the material by increasing the energy barrier for dislocation motion through the grain boundary rather than through the matrix. Consequently, precipitation strengthening would directly correlate to grain size strengthening mechanics. Within the scope of this project however, estimations from conventional Orowan looping are adequate.

Based on this information, multiple recommendations can be made on the general thermal treatment of 6061 powders.

1. Precipitation kinetics are hugely accelerated in the case of powders and typical treatments for casting cannot be assumed applicable
2. Specifically, high temperature treatment must be limited to discourage the coarsening on $\text{Al}_9\text{Fe}_2\text{Si}_2$ as precipitation and grain size strengthening have significant strengthening contributions
3. Precipitation hardening literature review should be focused on Q-AlCuMgSi, not Mg_2Si

To give context to point 3 above, and to illustrate the benefit of the validation process, Figure 13 displays the first run of precipitate estimations based on early work. These simulations focused on Mg_2Si and its corresponding metastable phases, based on literature review of typical 6061. This erroneous simulation was coupled with erroneous hardness measurements, seen in Figure 14.

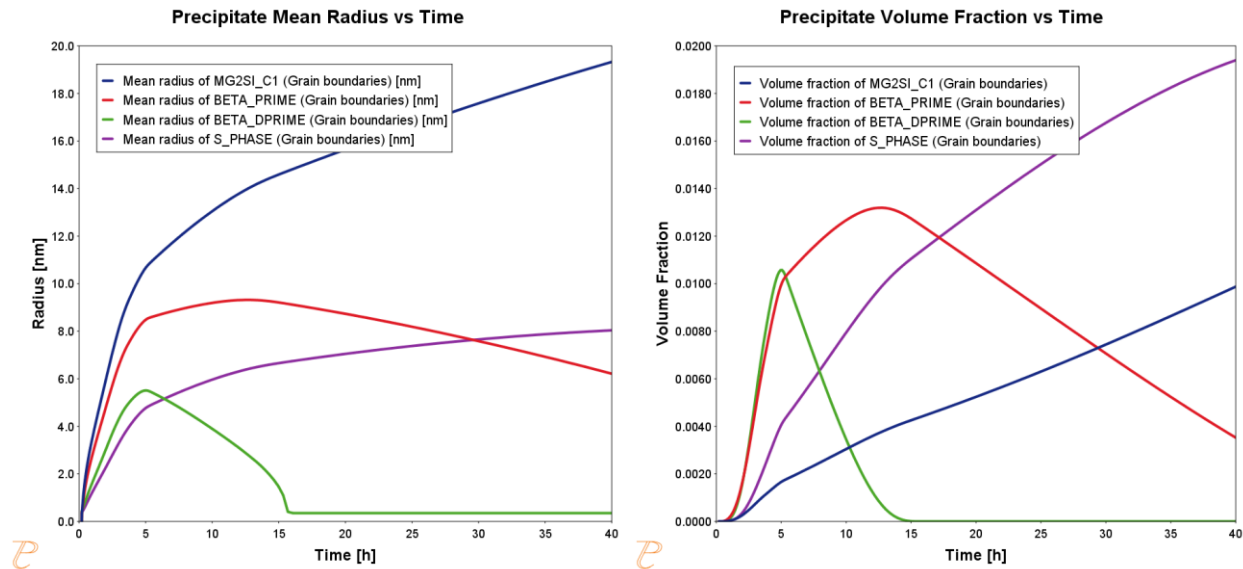


Figure 13: Precipitate modeling prior to validation steps

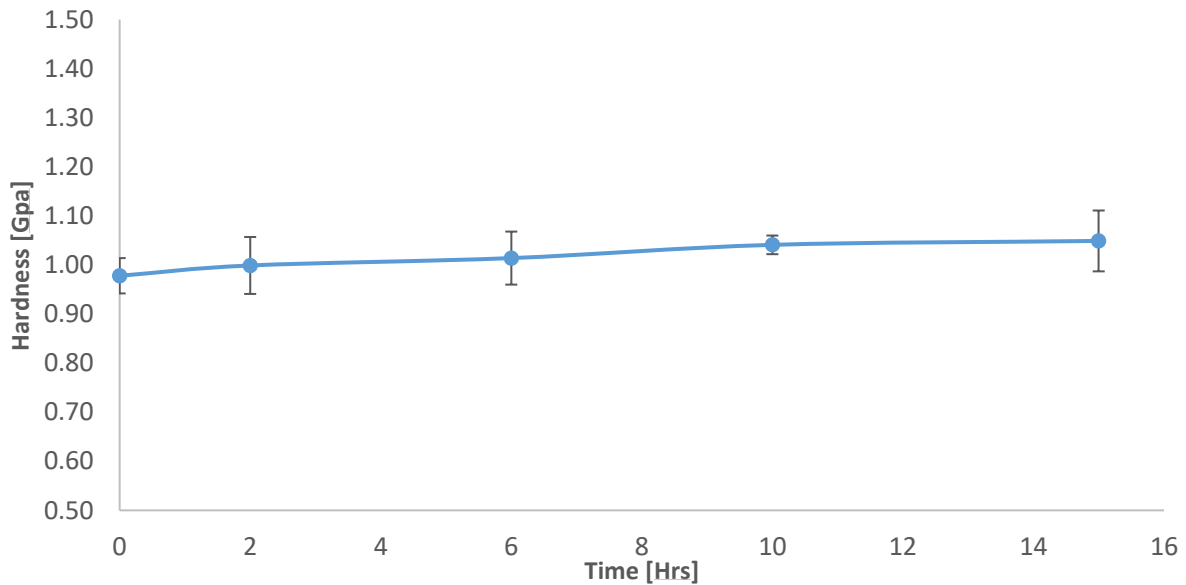


Figure 14: Hardness measurements prior to validation steps

As the scale of the Q-AlCuMgSi precipitates were too small to see in SEM, the only microscopy done in early work, a disconnect was observed between the precipitation expected via modeling and the lack of any hardening observed during hardness measurements. Through more intensive TEM, the models were able to be adjusted to match the actual microstructure; however, there was still a disconnect with the lack of hardness increases as that the strengthening model said there should be. This led to a reevaluation of our hardness measurement, where it was discovered that static testing was ineffectual for the accurate measurement of our systems. With proper dynamic testing, the true effect of the

changes in microstructure that both the simulations and the microscopy observed could be seen and correlated.

Through the use of the Iterative Experimental Model, an intrinsic understanding of the microstructural development of the Al 6061 system was obtained, as well as general correlations to yield strength and hardness. With this understanding, one can begin to optimize heat treatment parameters to develop microstructures with specific tailored properties, considering phase stability thresholds, growth and dissolution timelines, heating and cooling rate effects, and other adjustable parameters that would directly influence a powder's mechanical properties.

7.2. Relation to TPE

While a system was developed to predict microstructural changes as a function of heat treatment, a set of workable goals must be outlined to work towards before optimization can occur. Without additional studies directly applicable to cold spray, the knowledge described in this work is limited to what it can be applied to. As a result, the Through-Process Experiment was developed, using the information gathered to plan tests with specific goals in mind, enhancing the entire Design of Experiment (DoE). The ultimate goal of this project is to go beyond correlating powder heat treatments to just feedstock powder mechanical properties, but to also correlate powder heat treatments directly to cold spray characteristics and consolidated properties.

The batches and their respective goals will be listed below.

As-Received: Powder that has not been heat treated in anyway will be sprayed to analyze the influence of the eutectic-shaped $\text{Al}_{13}\text{Fe}_4$ and Mg_2Si network. Early sprays by ARL did not have much success without treating powders; however, it was assumed that the environmental effects were the main issue. As these powders will be inertly packaged, that confounding factor is removed.

De-Gassed: The general ARL-6061 process currently is a low temperature treatment to remove surface hydroxides. This treatment temperature is not high enough to influence either $\text{Al}_{13}\text{Fe}_4$ or Mg_2Si significantly based on computational models, therefore, the properties of this powder are expected to be comparable to the as-received. This batch will serve as a comparison point to recent studies performed by the ARL group. An example of this microstructure can be found in Figure 28.

Solutionized Short-Term: This batch will serve as a direct comparison to the Solutionized samples studied by the Cote group. Specifically, it will observe the effects of the transformation of $\text{Al}_{13}\text{Fe}_4$ to $\text{Al}_9\text{Fe}_2\text{Si}_2$ and the partial dissolution of Mg_2Si . Special attention will be put to the fracture mechanics of these samples, as the spherical precipitates are expected to behave much differently than the eutectic-shaped precipitates found in the as-received or de-gassed samples.

Solutionized Long-Term: These results will be directly compared to the results obtained from the "Solutionized Short-Term" batch. It will look at the influence of coarsening on $\text{Al}_9\text{Fe}_2\text{Si}_2$ and to determine if Mg_2Si will solutionize eventually. In the event that Mg_2Si does not solutionize, the further coarsening of this phase will be observed instead. Differences between the two solutionized batches will seek to provide concrete evidence that high temperature treatments should be limited for powders, whether from a decrease in mechanical performance or from the increased processing cost if the properties are comparable. An example of this microstructure can be found in Figure 29.

Solutionized and Aged: The final batch will observe the influence of the aged phases at the boundary. This will also serve to confirm Q-ALCuMgSi formation in a larger data set. For comparison to cast counterparts, the typical T6 treatment was chosen. Based on our preliminary results, it is expected to be in the overaged condition in the case of powders.

Through the combination of all five batches, specific characteristics will be analyzed. One of the most important conclusions this work will seek to achieve is the divergence of optimal short-term and long-term cold spray qualities. Good short-term qualities would include anything related to “sprayability,” being able to create non-porous, uniform coatings efficiently through good flowability and deposition rates. Generally, the more ductile a powder is, the better it deposits. However, that ductility must be balanced to its strength, otherwise it makes more sense to spray pure metals rather than an alloy. This relationship has not been fully developed previously. Additionally, certain microstructural features may respond better to the rapid increase in dislocation density. For example, as seen in Table 1, the hardness of the solutionized and 10 hour aged samples were relatively similar, but the way that these strengths were achieved were different. A solute-rich matrix may behave differently than a precipitate rich one under intense deformation, which is initially evident based off the differing moduli.

Long-term qualities relate with the material after it has been already sprayed. Ductility that was desired for good deposition may not be desirable for a wear resistance coating. Coarse precipitates that resulted from certain thermal treatments may have serious ramifications in terms fracture properties, as previously discussed. Certain microstructures may maintain their strength much better in the event of stress relaxation or elevated thermal conditions. These factors must be separated from short-term ones so that the desirable properties for a given situation can be outlined and worked towards. As short-term problems may be able to be bypassed by other methods, such atomization or cold spray equipment improvements, the long-term problems can be directly addressed. While not considered in the Through-Process Experiment presently, properties such as creep, fatigue resistance, and corrosion resistance would also play a much more important role as the technology continues to develop.

8. Conclusion

Using this Al-6061 case study in reference to the Iterative Experimental Model, the combination of computational modeling and experimental work was able to characterize and fully understand a system that did not have previous specific literature data to fall back on. The initial simulations allowed for a “flashlight” to be shown upon this system, quickening the overall process of microstructure identification. By validating and calibrating the simulations with data drawn from characterization, further understanding of powder precipitation thermodynamics were elaborated on. With these validated models, information could be extrapolated on that would allow insight on situations that were not specifically characterized, such as slight variations in composition or the variation of time/temperature. In order to directly correlate the microstructural features to cold spray characteristics, the Through-Process Experiment was developed. Using the validated models, points of interest were determined that will enable ARL to develop situation-specific powder that is reliable and repeatable. These conclusions will also aid in the understanding of alloy systems, creating the intrinsic feature correlations needed to develop optimal consolidated materials.

9. Future Work

In the future, Through-Process Experiments and Iterative Experimental Models will expand to include different batch initial conditions, other alloy systems, and additional mechanical properties. As these projects are concluded, including the one described here in the work, the data will be used to further understand the interplay between specific parameters and their overall effect on the cold spray process. With this understanding, the Through-Process Model will be expanded upon, enabling the prediction of consolidated properties through computational means, allowing for optimized properties and expediting the materials design and qualification process.

10. References

- [1] T. Griger, "Materials Acceleration Platform: Accelerating Advanced Energy Materials Discovery by Integrating High-Throughput Methods and Artificial Intelligence."
- [2] D. Belsito, B. McNally, L. Bassett, R. Sisson, and V. Champagne, "A through-process model for cold sprayed aluminum alloys," in *Thermal Process Modeling - Proceedings from the 5th International Conference on Thermal Process Modeling and Computer Simulation, ICTPMCS 2014*, 2014, pp. 308–314.
- [3] D. Belsito, "Application of Computational Thermodynamic and Solidification Kinetics to Cold Sprayable Powder Alloy Design," 2014.
- [4] V. K. Champagne, *The cold spray materials deposition process : fundamentals and applications*. Woodhead, 2007.
- [5] V. K. Champagne, "The Repair of Magnesium Rotorcraft Components by Cold Spray," *J. Fail. Anal. Prev.*, vol. 8, no. 2, pp. 164–175, Apr. 2008.
- [6] W. A. Story and L. N. Brewer, "Heat Treatment of Gas-Atomized Powders for Cold Spray Deposition," *Metall. Mater. Trans. A*, vol. 49, no. 2, pp. 446–449, Feb. 2018.
- [7] A. Sabard, ... H. de V. L.-J. of T. S., and undefined 2018, "Microstructural evolution in solution heat treatment of gas-atomized Al alloy (7075) powder for cold spray," *Springer*.
- [8] H. Lukas, S. Fries, and B. Sundman, *Computational thermodynamics: the Calphad method*. 2007.
- [9] A. Borgenstam, L. Höglund, J. Ågren, and A. Engström, "DICTRA, a tool for simulation of diffusional transformations in alloys," *J. Phase Equilibria*, vol. 21, no. 3, pp. 269–280, May 2000.
- [10] Z. C. Cordero, B. E. Knight, and C. A. Schuh, "Six decades of the Hall-Petch effect-a survey of grain-size strengthening studies on pure metals FULL CRITICAL REVIEW Six decades of the Hall-Petch effect-a survey of grain-size strengthening studies on pure metals," 2016.
- [11] R. . Fleischer, "Substitutional solution hardening," *Acta Metall.*, vol. 11, no. 3, pp. 203–209, Mar. 1963.
- [12] R. . Fleisgher, "Solution hardening," *Acta Metall.*, vol. 9, no. 11, pp. 996–1000, Nov. 1961.
- [13] T. Courtney, *Mechanical behavior of materials*. 2005.

- [14] K. Ma *et al.*, "Mechanical behavior and strengthening mechanisms in ultrafine grain precipitation-strengthened aluminum alloy," *Acta Mater.*, vol. 62, no. 1, pp. 141–155, 2014.
- [15] K. Tsaknopoulos, C. Walde, V. C. Jr, and D. Cote, "Gas-Atomized Al 6061 Powder : Phase Identification and Evolution During Thermal Treatment," *JOM*, 2018.
- [16] E. J.R. Davis, *Aluminum and Aluminum Alloys*, *ASM Specialty Handbook*. ASM International, 1993.
- [17] J. M. Schreiber, "Finite Element Implementation of the Preston-Tonks-Wallace Plasticity Model and Energy Based Bonding Parameter for the Cold Spray Process." 2016.
- [18] O. C. Ozdemir, C. A. Widener, M. J. Carter, and K. W. Johnson, "Predicting the Effects of Powder Feeding Rates on Particle Impact Conditions and Cold Spray Deposited Coatings," *J. Therm. Spray Technol.*, vol. 26, no. 7, pp. 1598–1615, Oct. 2017.
- [19] Q. Chen *et al.*, "High-Strain-Rate Material Behavior and Adiabatic Material Instability in Impact of Micron-Scale Al-6061 Particles," *J. Therm. Spray Technol.*, vol. 27, no. 4, pp. 641–653, Apr. 2018.
- [20] S. Suresh, S.-W. Lee, M. Aindow, H. D. Brody, V. K. Champagne, and A. M. Dongare, "Unraveling the Mesoscale Evolution of Microstructure during Supersonic Impact of Aluminum Powder Particles," *Sci. Rep.*, vol. 8, no. 1, p. 10075, Dec. 2018.
- [21] B. A. Bedard *et al.*, "Microstructure and Micromechanical Response in Gas-Atomized Al 6061 Alloy Powder and Cold-Sprayed Splats," *J. Therm. Spray Technol.*, vol. 27, no. 8, pp. 1563–1578, Dec. 2018.
- [22] M. Hassani-Gangaraj, D. Veysset, K. A. Nelson, and C. A. Schuh, "In-situ observations of single micro-particle impact bonding," *Scr. Mater.*, vol. 145, pp. 9–13, Mar. 2018.
- [23] P. Nautiyal, C. Zhang, V. K. Champagne, B. Boesl, and A. Agarwal, "In-situ mechanical investigation of the deformation of splat interfaces in cold-sprayed aluminum alloy," *Mater. Sci. Eng. A*, vol. 737, pp. 297–309, Nov. 2018.
- [24] C. Walde, D. Cote, V. Champagne, and R. Sisson, "Characterizing the Effect of Thermal Processing on Feedstock Al Alloy Powder for Additive Manufacturing Applications," *J. Mater. Eng. Perform.*, pp. 0–9, 2018.
- [25] A. Polat, M. Avsar, and F. Ozturk, "EFFECTS OF THE ARTIFICIAL-AGING TEMPERATURE AND TIME ON THE MECHANICAL PROPERTIES AND SPRINGBACK BEHAVIOR OF AA6061 VPLIV TEMPERATURE IN ^ASA UMETNEGA STARANJA NA MEHANSKE LASTNOSTI IN VZMETNOST AA6061."

11. Appendix A: Figures

11.1. Models

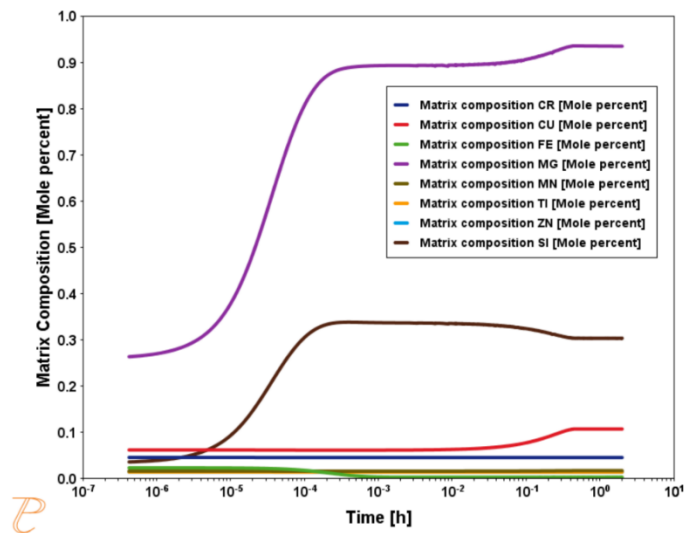


Figure 15: "Solutionized" matrix composition as a function of time at 530°C for Al 6061 using Thermo-Calc precipitation module

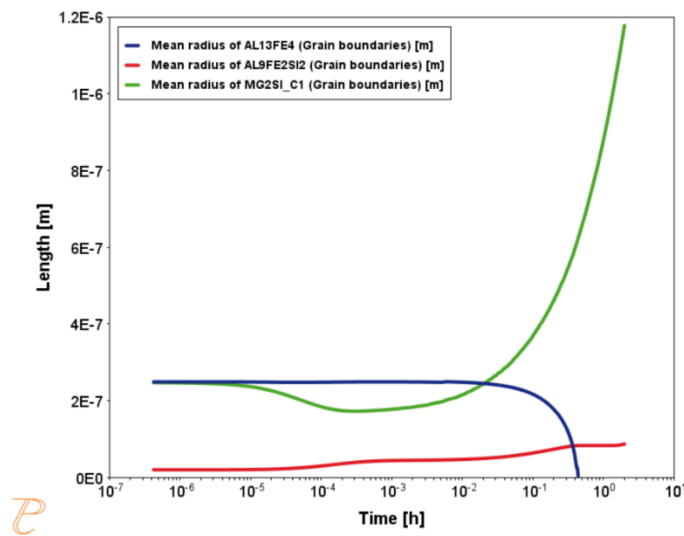


Figure 16: "Solutionized" precipitate mean radius as a function of time at 530°C for Al 6061 using Thermo-Calc precipitation module

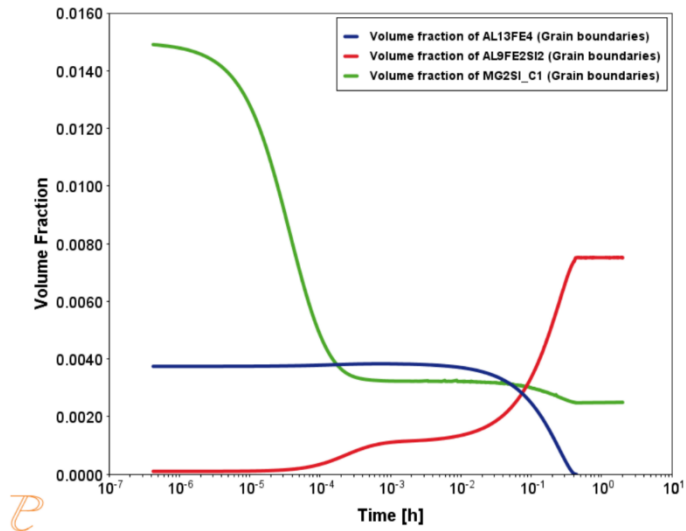


Figure 17: "Solutionized" precipitate volume fraction as a function of time at 530°C for Al 6061 using Thermo-Calc precipitation module

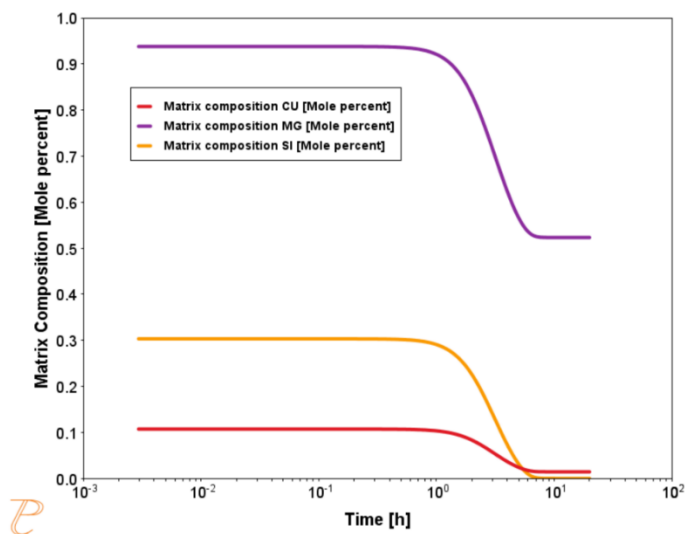


Figure 18: "Aged" matrix composition as a function of time at 170°C for Al 6061 using Thermo-Calc precipitation module

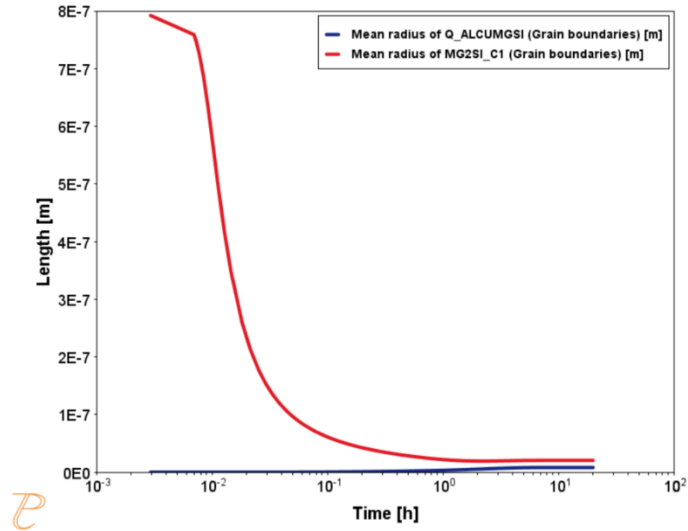


Figure 19: "Aged" precipitate mean radius as a function of time at 170°C for Al 6061 using Thermo-Calc precipitation module

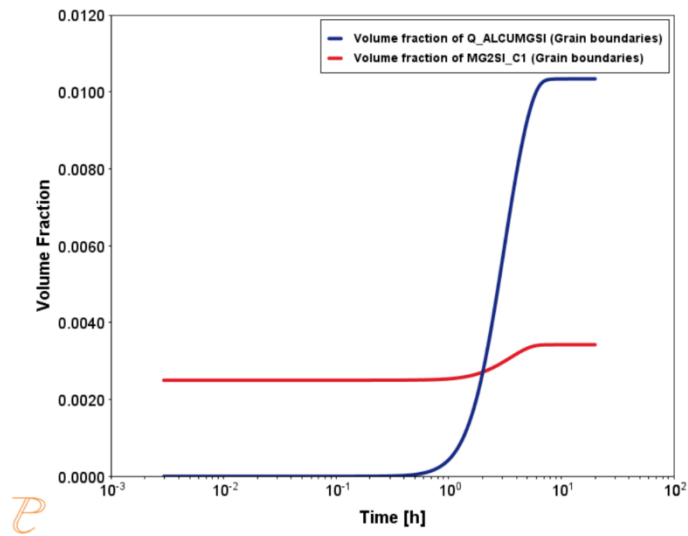


Figure 20: "Aged" precipitate volume fraction as a function of time at 170°C for Al 6061 using Thermo-Calc precipitation module

11.1.1.Settings

The screenshot shows the 'System Definer 3' window in Thermo-Calc. The 'Databases' section includes 'TCAL6: Al-Alloys v6.0' and 'MOBAL5: Al-Alloys Mobility v5.0'. The 'Elements' tab is active, showing a periodic table with several elements highlighted in blue: Ti, Cr, Mn, Fe, Cu, Zn, Al, and Si. A 'Material' panel on the right shows the material name '6061' and a list of elements with their mole percentages:

Element	Amount (Mole percent)
Al	98.143
Cr	0.045
Cu	0.106
Fe	0.131
Mg	1.058
Mn	0.017
Ti	0.014
Zn	0.014
Si	0.472

At the bottom of the window, there are buttons for 'Help', 'Add Predecessor', 'Perform Tree', and 'Create New Successor'.

Figure 21: Thermo-Calc System Definer example for Al 6061

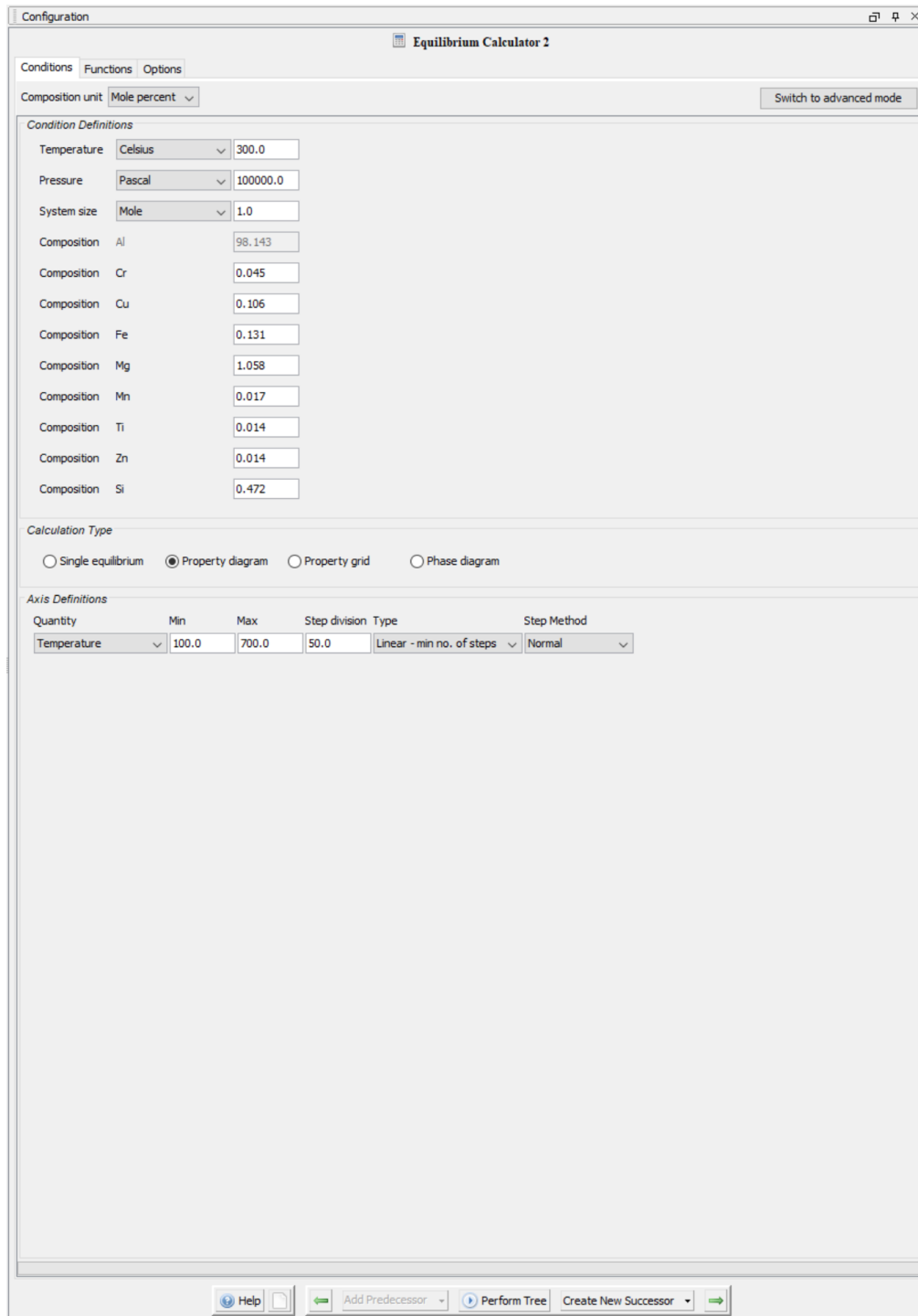


Figure 22: Thermo-Calc Equilibrium Calculator example for Al 6061. Used for generation of Figure 8

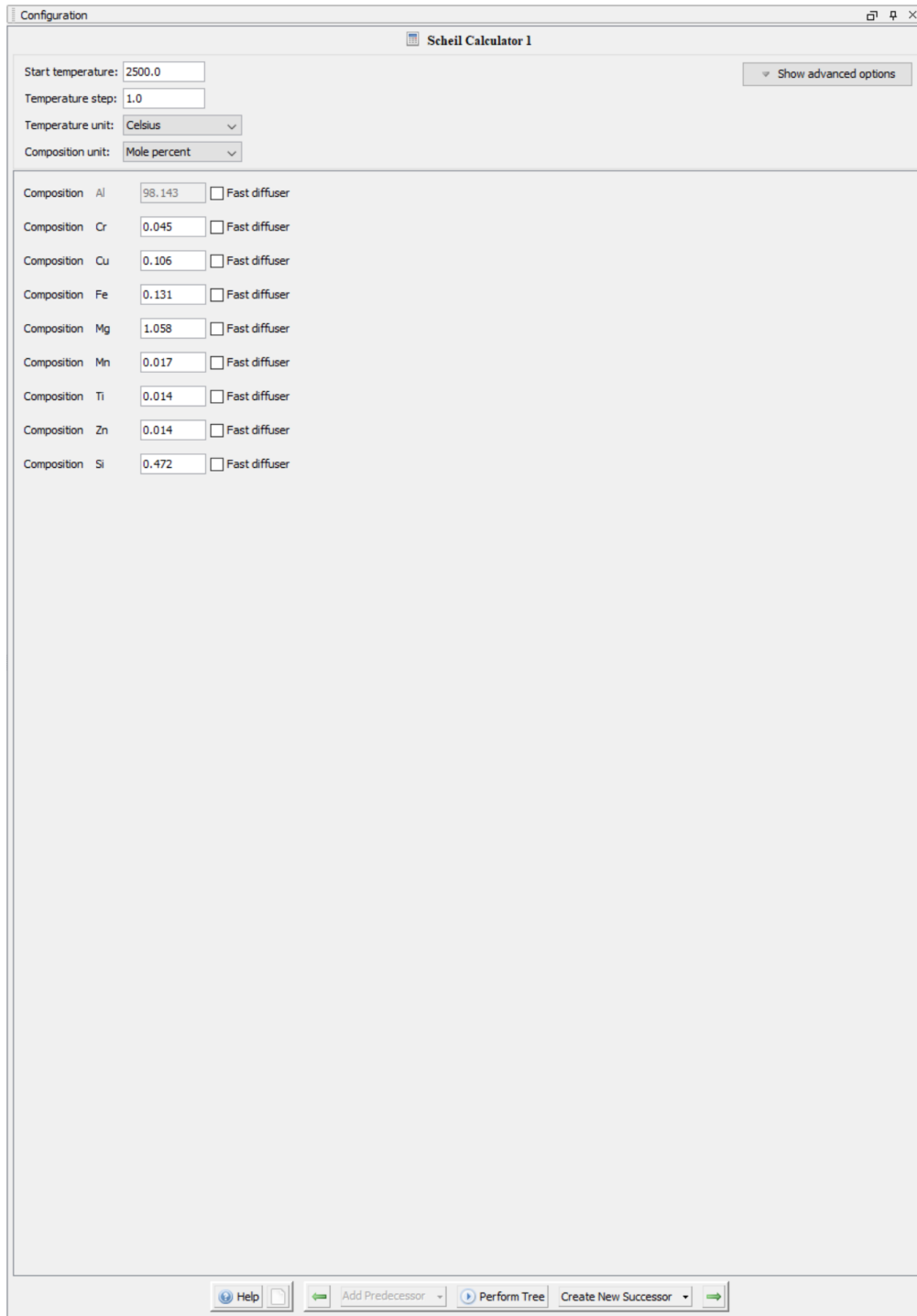


Figure 23: Thermo-Calc Scheil Calculator example for Al 6061. Used for generation of Figure 6

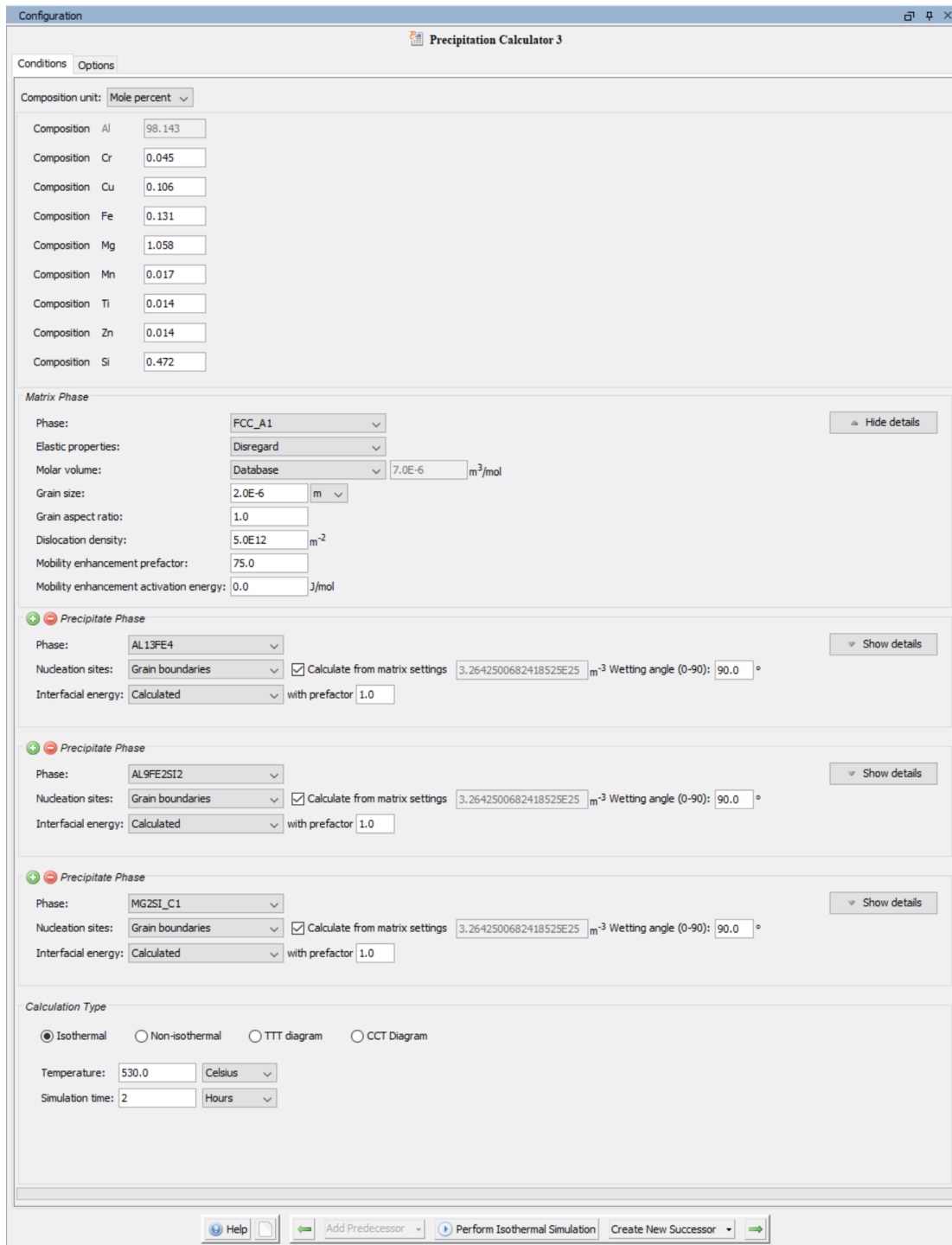


Figure 24: Thermo-Calc Precipitation Calculator example for Al 6061. Used for generation of "Solutionized" precipitate models

Precipitate Phase

Phase: AL13FE4 Hide details

Nucleation sites: Grain boundaries Calculate from matrix settings $3.2642500682418525E25$ m⁻³ Wetting angle (0-90): 90.0 °

Interfacial energy: Calculated with prefactor 1.0

Growth rate model: Simplified

Morphology: Sphere

Transformation strain: Disregard

Molar volume: Database 7.0E-6 m³/mol

Phase boundary mobility: 10.0 m⁴/Js

Phase energy addition: 0.0 J/mol

Approximate driving force:

Preexisting size distribution: Edit particle size distribution

Precipitate Phase

Phase: AL9FE2SI2 Hide details

Nucleation sites: Grain boundaries Calculate from matrix settings $3.2642500682418525E25$ m⁻³ Wetting angle (0-90): 90.0 °

Interfacial energy: Calculated with prefactor 1.0

Growth rate model: Simplified

Morphology: Sphere

Transformation strain: Disregard

Molar volume: Database 7.0E-6 m³/mol

Phase boundary mobility: 10.0 m⁴/Js

Phase energy addition: 0.0 J/mol

Approximate driving force:

Preexisting size distribution: Edit particle size distribution

Precipitate Phase

Phase: MG2SI_C1 Hide details

Nucleation sites: Grain boundaries Calculate from matrix settings $3.2642500682418525E25$ m⁻³ Wetting angle (0-90): 90.0 °

Interfacial energy: Calculated with prefactor 1.0

Growth rate model: Simplified

Morphology: Sphere

Transformation strain: Disregard

Molar volume: Database 7.0E-6 m³/mol

Phase boundary mobility: 10.0 m⁴/Js

Phase energy addition: -1400.0 J/mol

Approximate driving force:

Preexisting size distribution: Edit particle size distribution

Figure 25: Expanded Thermo-Calc Precipitation Calculator precipitate settings

11.2. Microscopy

11.2.1. Scanning Electron Microscopy

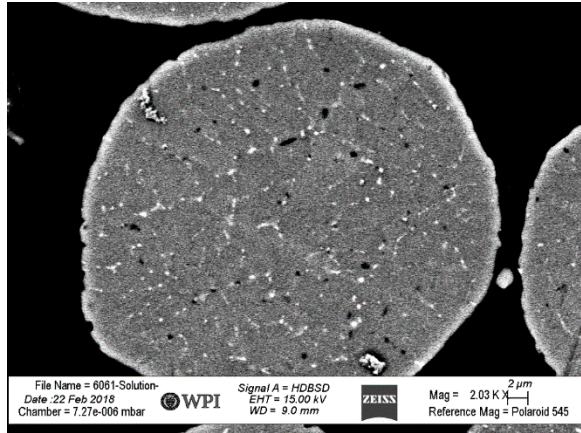


Figure 26: SEM of Solutionized-6061

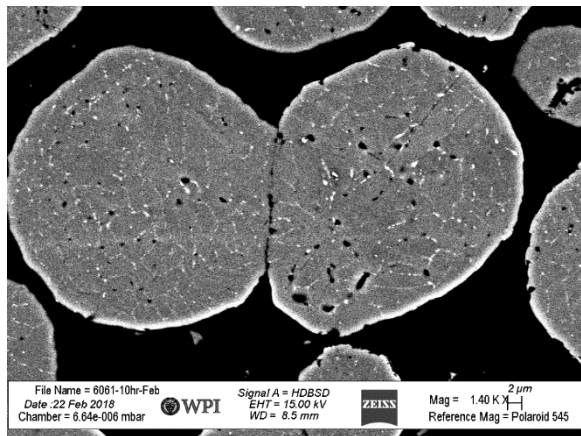


Figure 27: SEM of 10 hour aged-6061

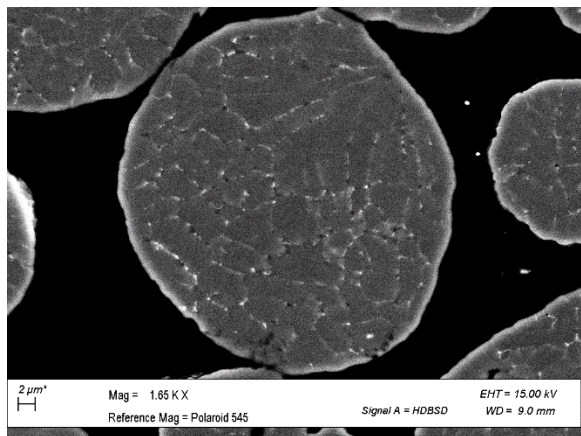


Figure 28: SEM of De-Gassed 6061

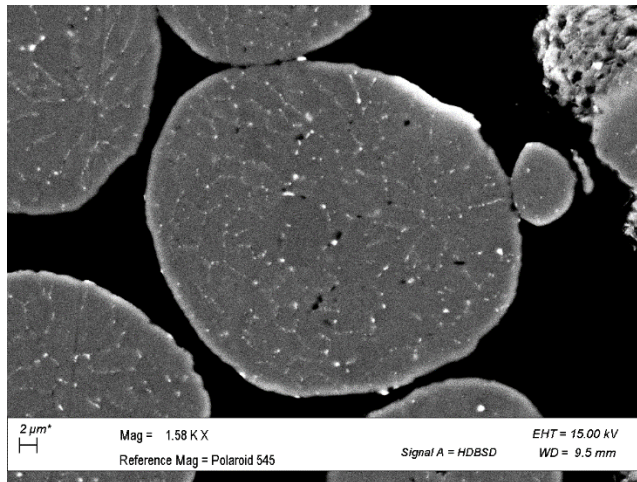


Figure 29: SEM of Over-Solutionized 6061

11.2.2. Scanning Transmission Electron Microscopy-Energy Dispersive Spectroscopy w/ Diffraction

11.2.2.1. As-received

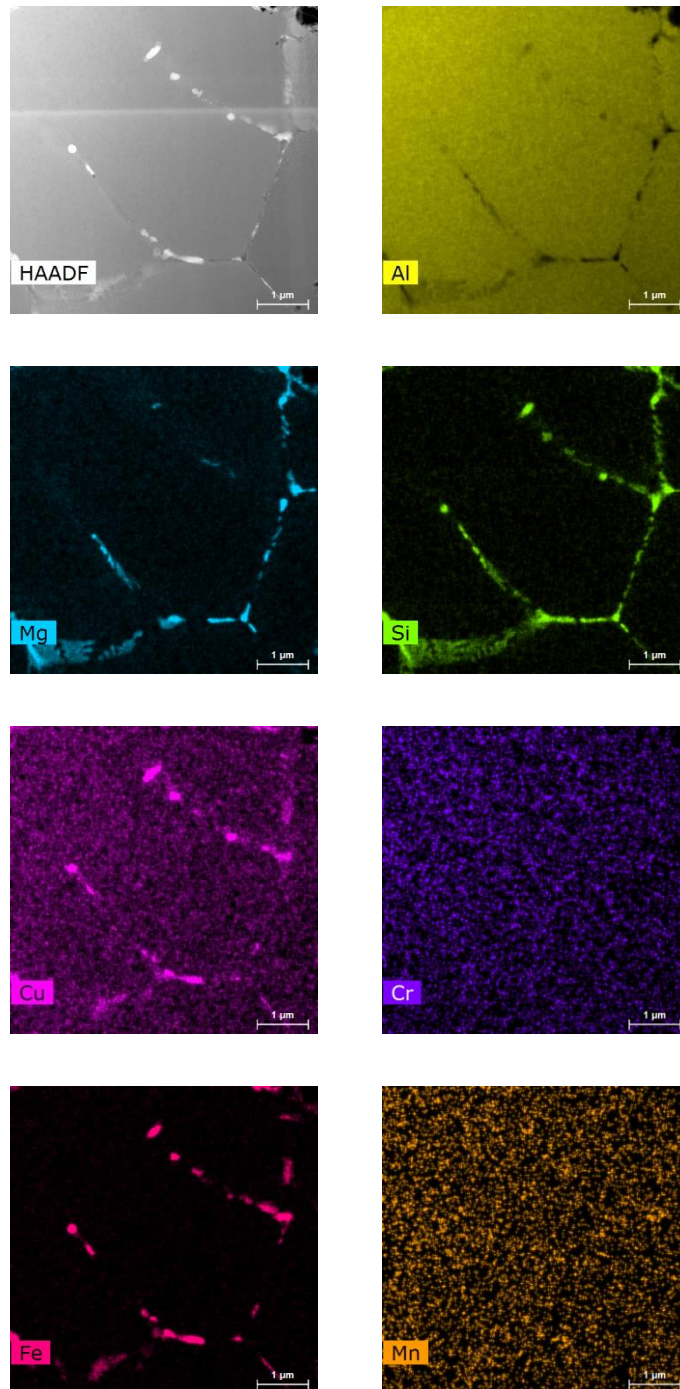


Figure 30: STEM-EDS of AR-6061 performed by Ballie McNally (Haddad)

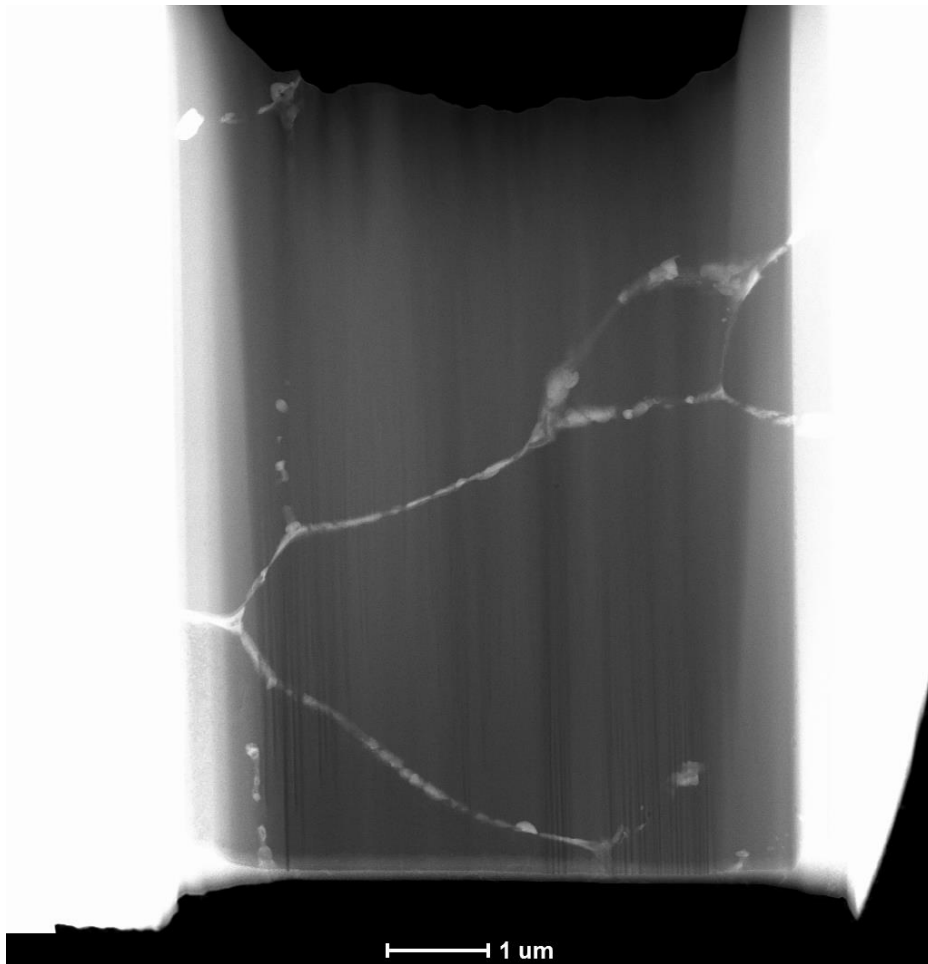


Figure 31: HAADF of AR-6061 performed by Caitlin Walde and Kyle Tsaknopoulos

11.2.2.2. Solutionized

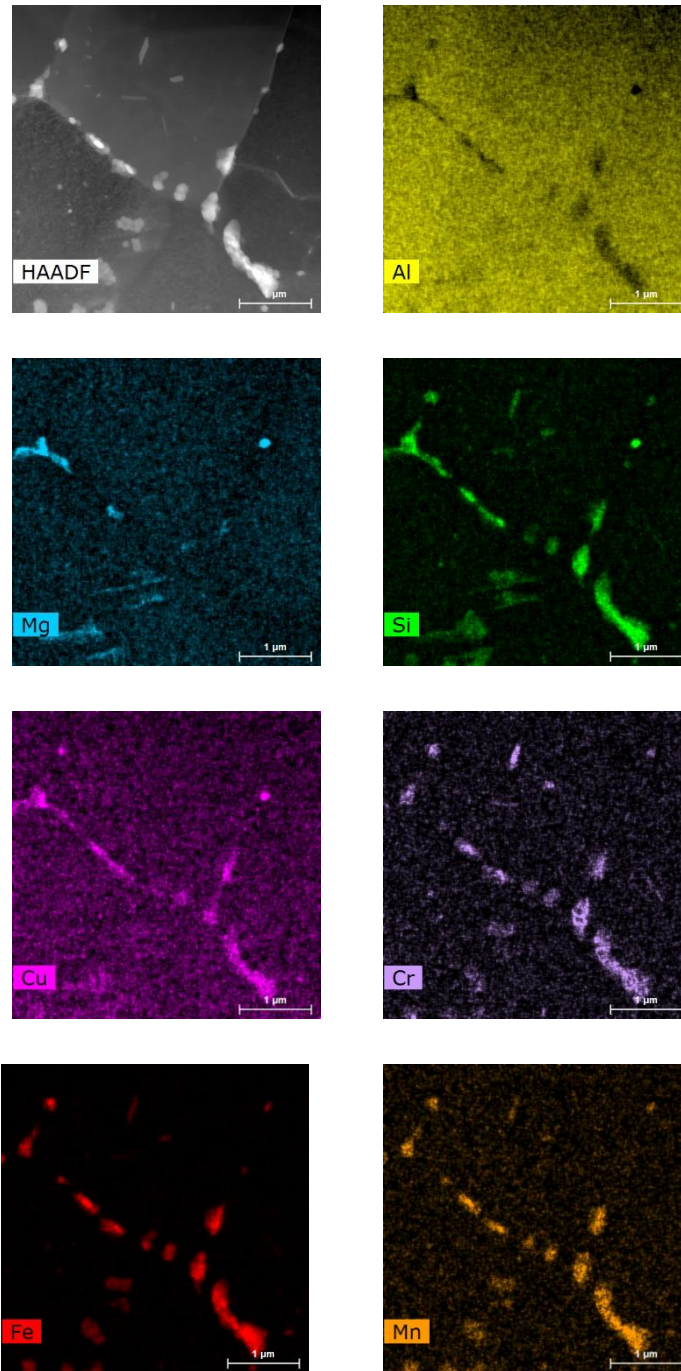


Figure 32: STEM-EDS of Solutionized-6061 performed by Ballie McNally (Haddad)

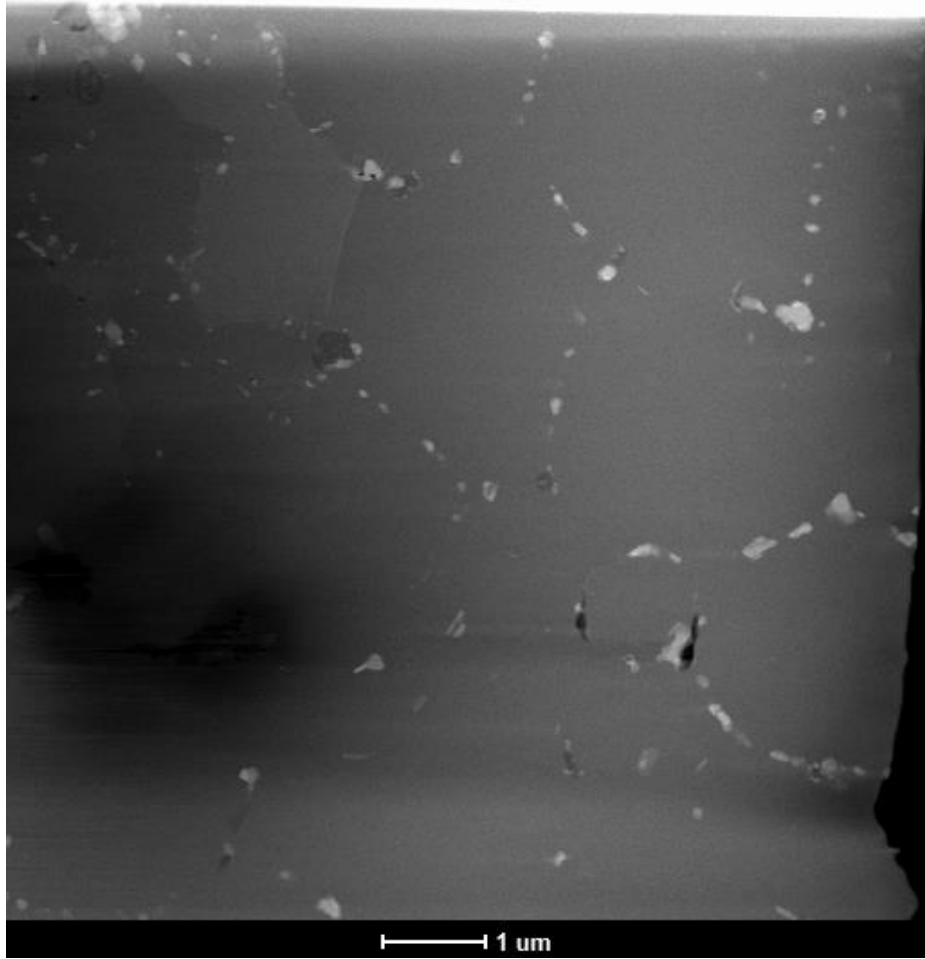


Figure 33: HAADF of Solutionized-6061 performed by Caitlin Walde and Kyle Tsakopoulos

11.2.2.3. Aged

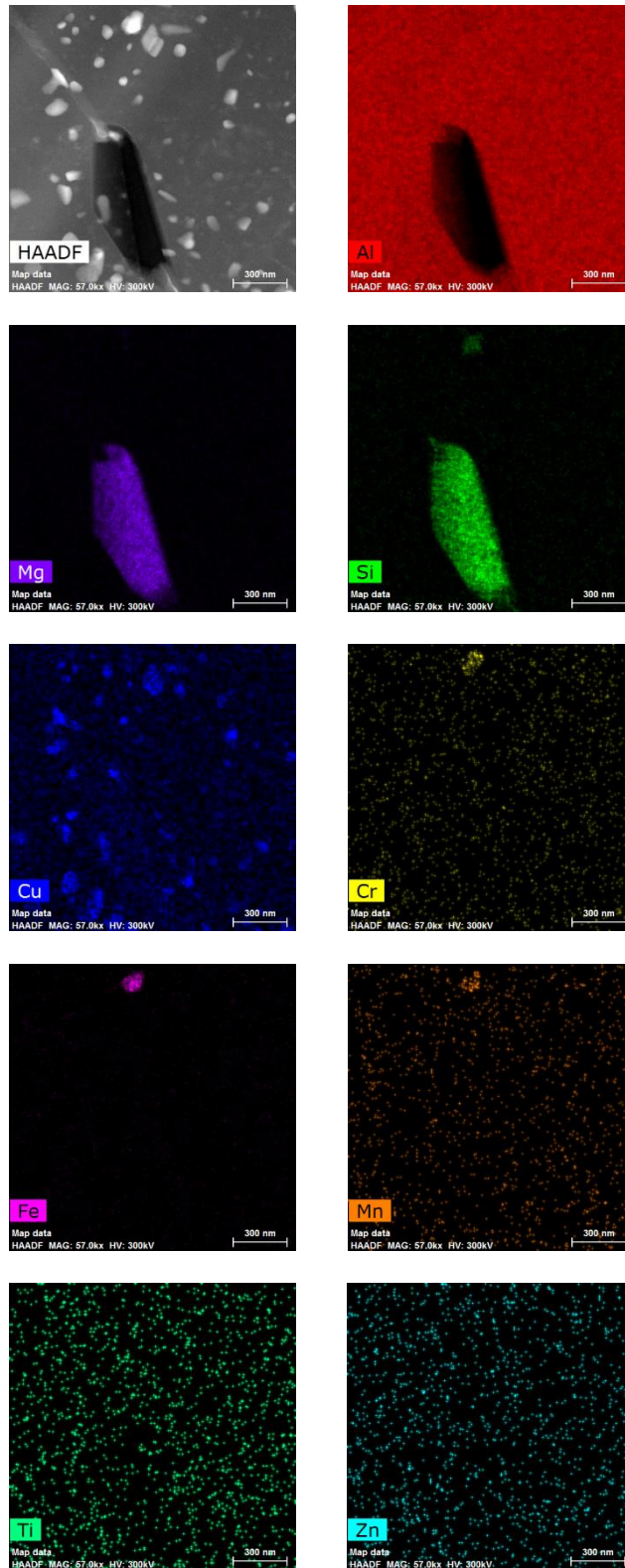


Figure 34: STEM-EDS of 4 Hour aged-6061

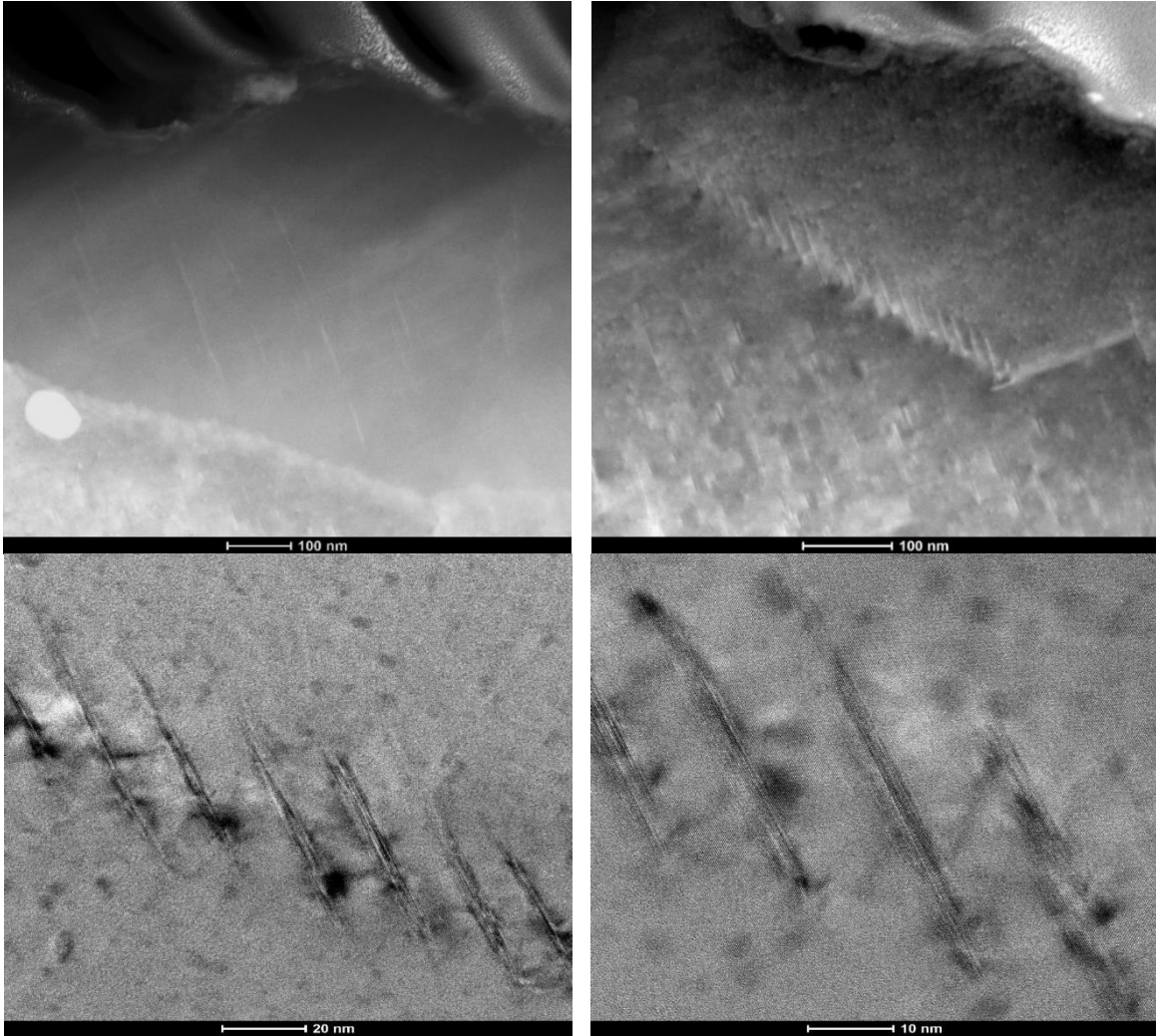


Figure 35: HAADF of 8 Hour aged-6061

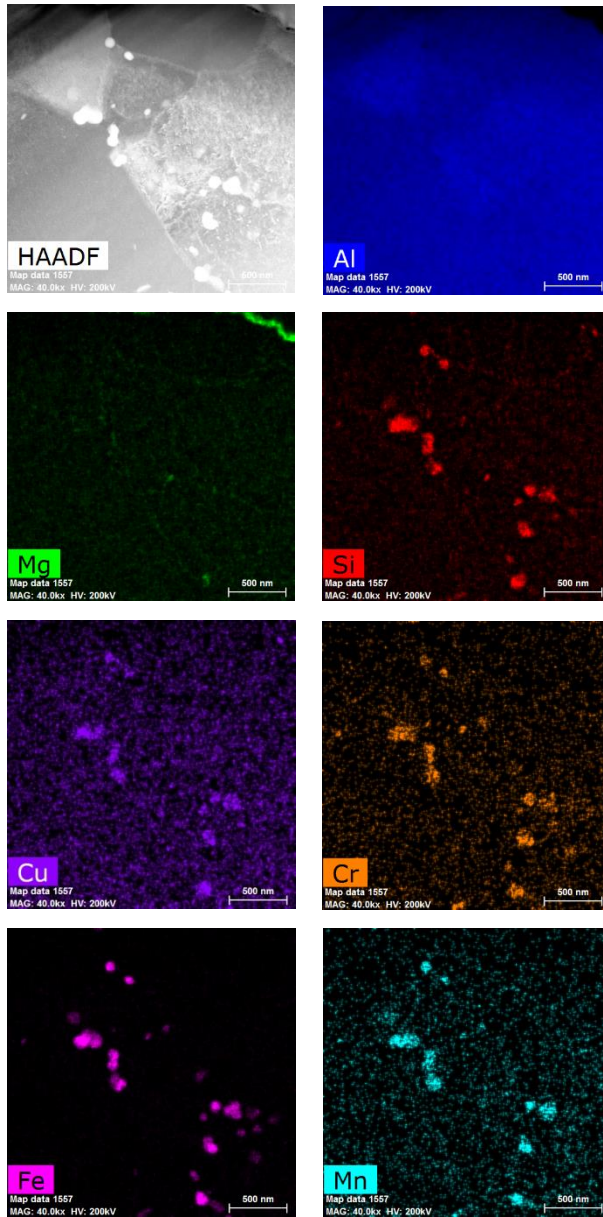


Figure 36: Low Mag STEM-EDS of 8 Hour Aged-6061 performed by PSU Applied Research Laboratory

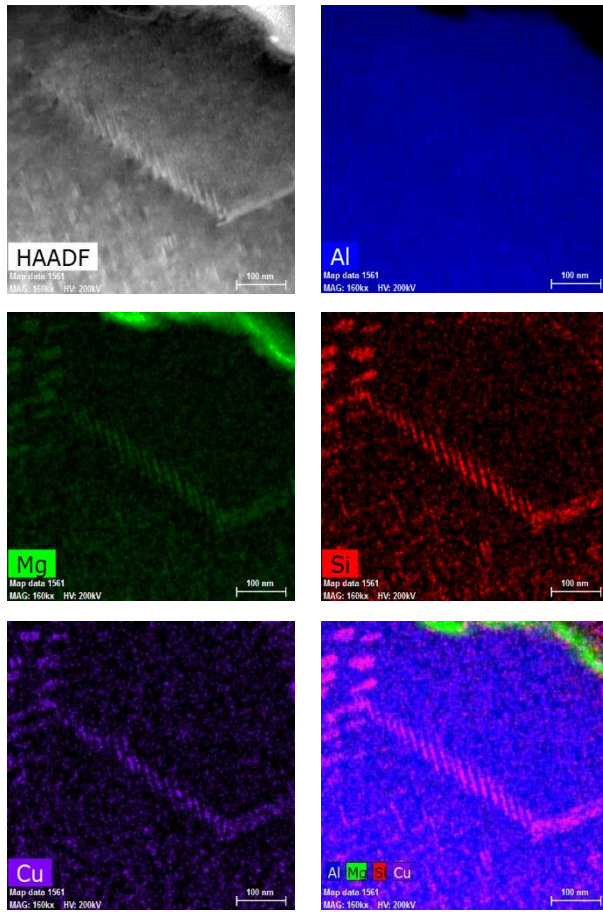


Figure 37 High Mag STEM-EDS of 8 Hour Aged-6061 performed by PSU Applied Research Laboratory

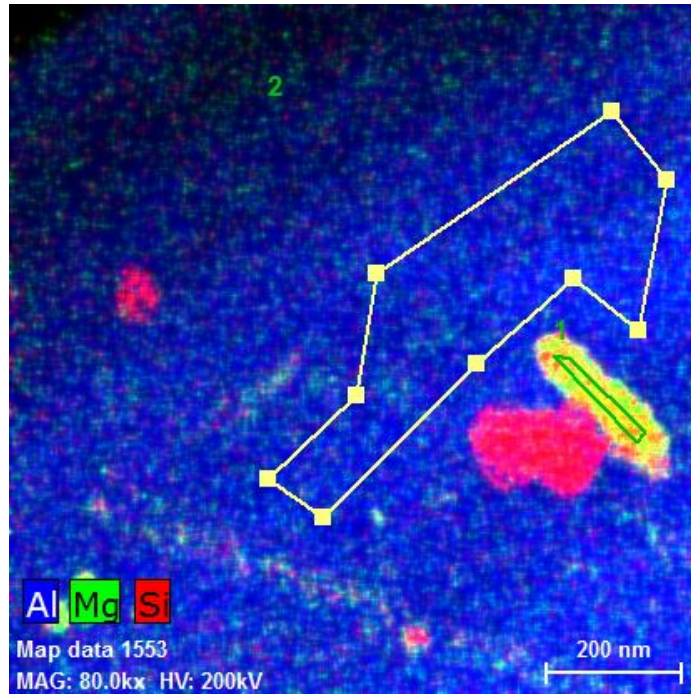


Figure 38: STEM-EDS quantifications of 8 Hour Aged-6061 performed by PSU Applied Research Laboratory

Table 2: Elemental quantifications of Particle region found in Figure 38

Element	series	[norm. wt.%]	[norm. at.%]	(3 Sigma)
Aluminium	K-series	58.53	60.08	6.56
Magnesium	K-series	13.68	15.59	2.22
Silicon	K-series	13.46	13.27	1.90
Oxygen	K-series	3.01	5.22	1.01
Copper	K-series	10.51	4.58	2.45
Carbon	K-series	0.47	1.08	0.54
Manganese	K-series	0.23	0.12	0.36
Chromium	K-series	0.11	0.06	0.27
		100	100	

Table 3: Elemental quantifications of Matrix found in Figure 38

Element	series	[norm. wt.%]	[norm. at.%] (3 Sigma)	
Aluminium	K-series	94.93	92.33	8.65
Oxygen	K-series	3.83	6.28	0.45
Magnesium	K-series	0.57	0.61	0.15
Carbon	K-series	0.28	0.60	0.14
Copper	K-series	0.27	0.11	0.13
Iron	K-series	0.10	0.05	0.11
Chromium	K-series	0.02	0.01	0.09
Manganese	K-series	0.01	0.00	0.08
Silicon	K-series	0.00	0.00	0.08
		100	100	



Figure 39: Diffraction pattern of "cross-hatched" region found in bottom left of image of Figure 37

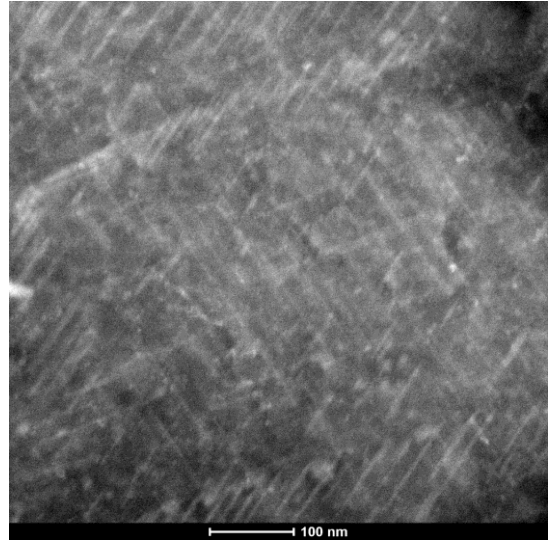


Figure 40: HAADF of 25 Hour Aged-6061 performed by PSU Applied Research Laboratory

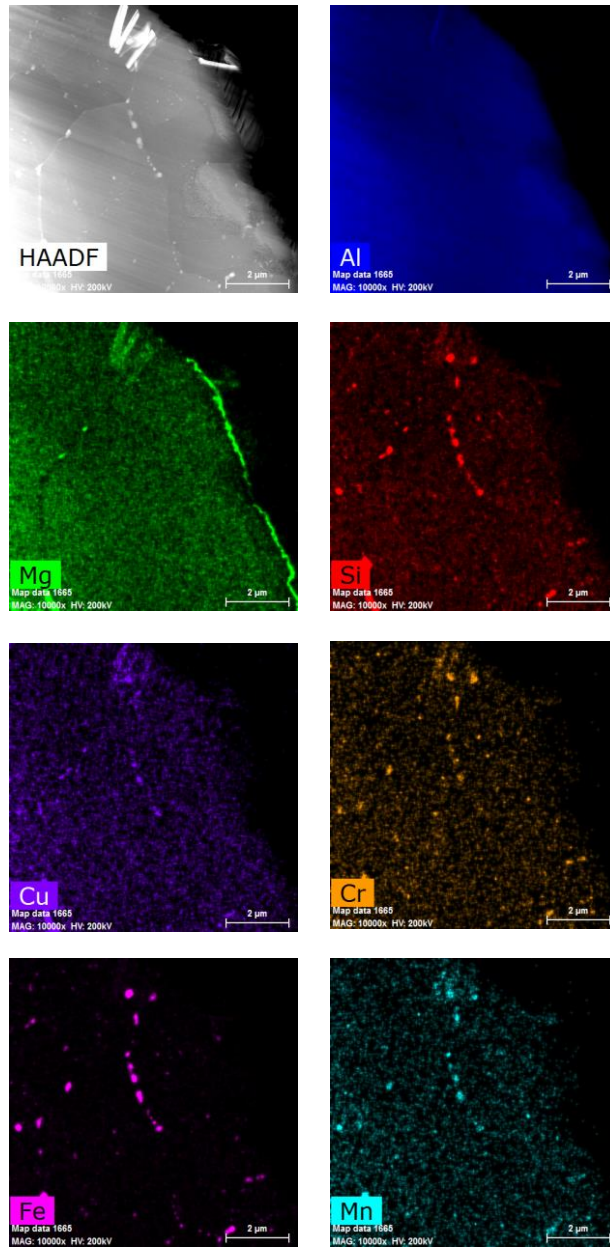


Figure 41: Low Mag STEM-EDS of 25 Hour Aged-6061 performed by PSU Applied Research Laboratory

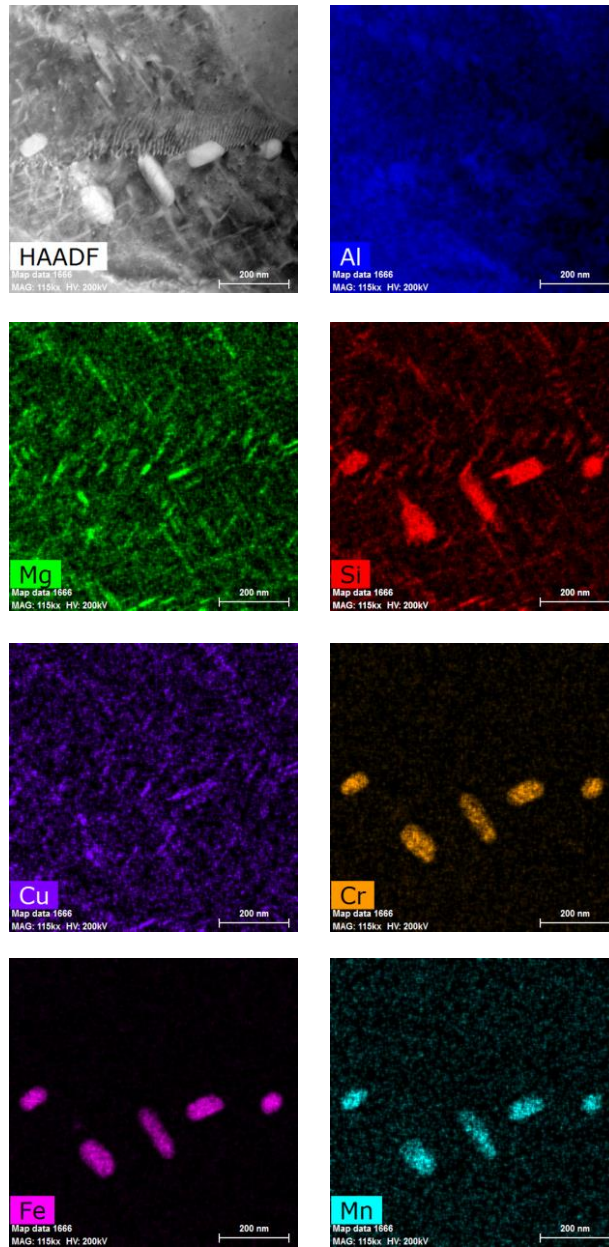


Figure 42: High Mag STEM-EDS of 25 Hour Aged-6061 performed by PSU Applied Research Laboratory

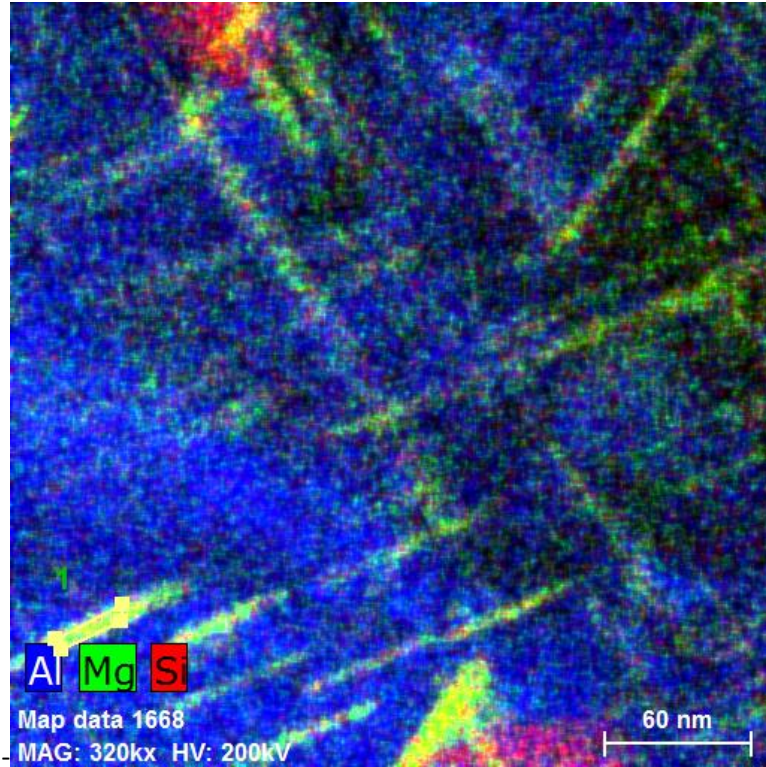


Figure 43: High Mag STEM-EDS overlay of 25 Hour Aged-6061 performed by PSU Applied Research Laboratory

Table 4: Elemental quantification of lathe-like precipitate found in Figure 43

Element	Series	Net	Mass C. [wt.%]	norm. C. [wt.%]	Atom C. [at.%]	Error (3 Sigma) [wt.%]
Al	K series	5294	77.04	84.25	83.23	7.71
O	K series	85	1.38	1.51	2.52	0.54
C	K series	40	1.13	1.24	2.75	0.62
Mg	K series	369	5.03	5.50	6.04	0.98
Cu	K series	120	2.83	3.10	1.30	0.95
Si	K series	283	4.02	4.40	4.17	0.81
		Total	91.44	100.00	100.00	

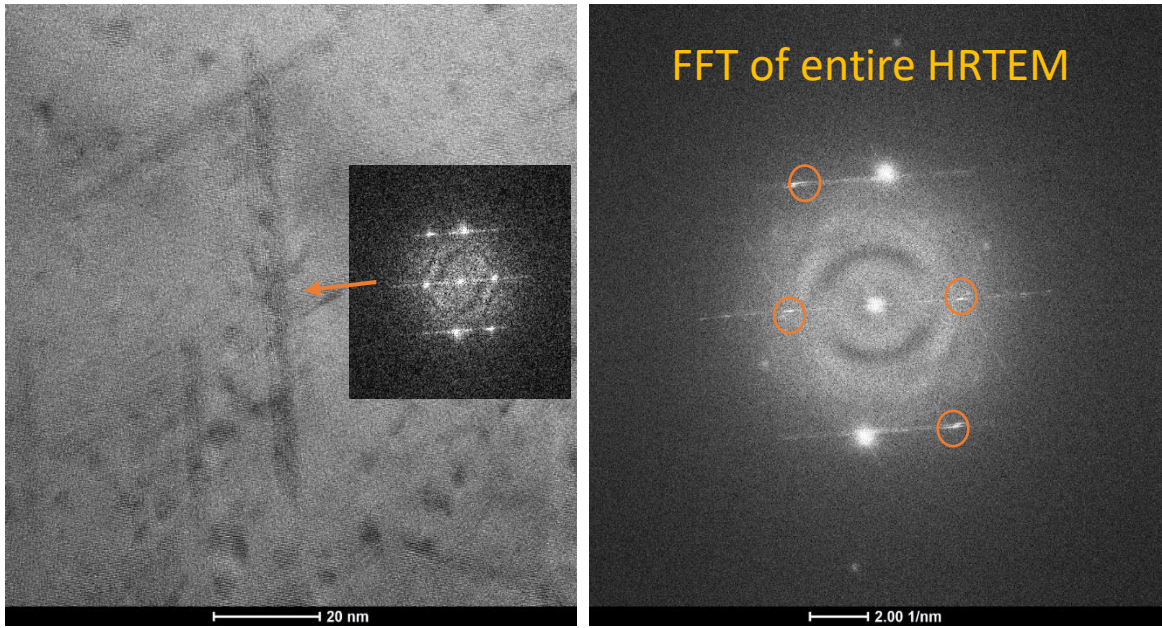


Figure 44: HAADF and diffraction pattern of lathe-like precipitate in 25 Hour Aged-6061 performed by PSU Applied Research Laboratory

11.3. Nanoindentation

11.3.1. As-received

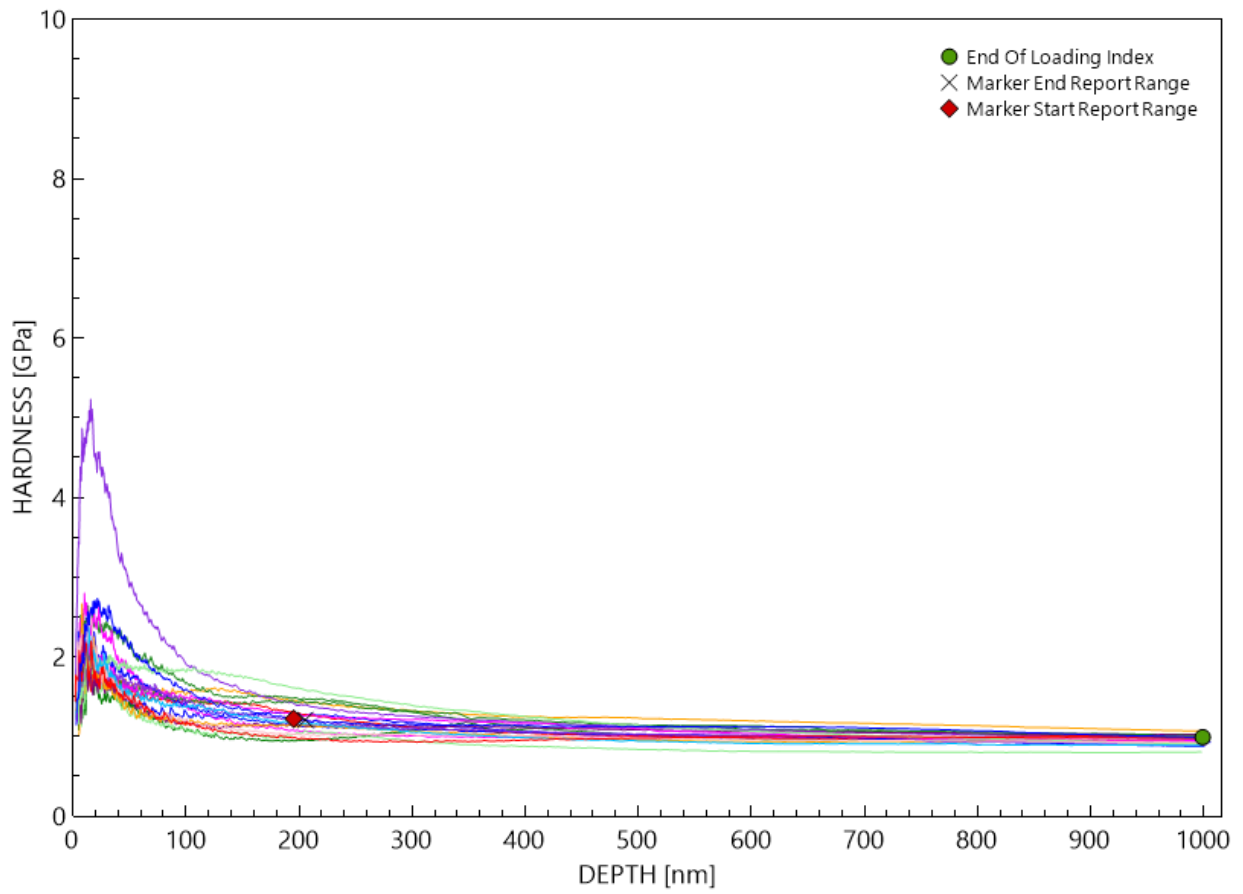


Figure 45: Hardness vs Depth data for AR-6061

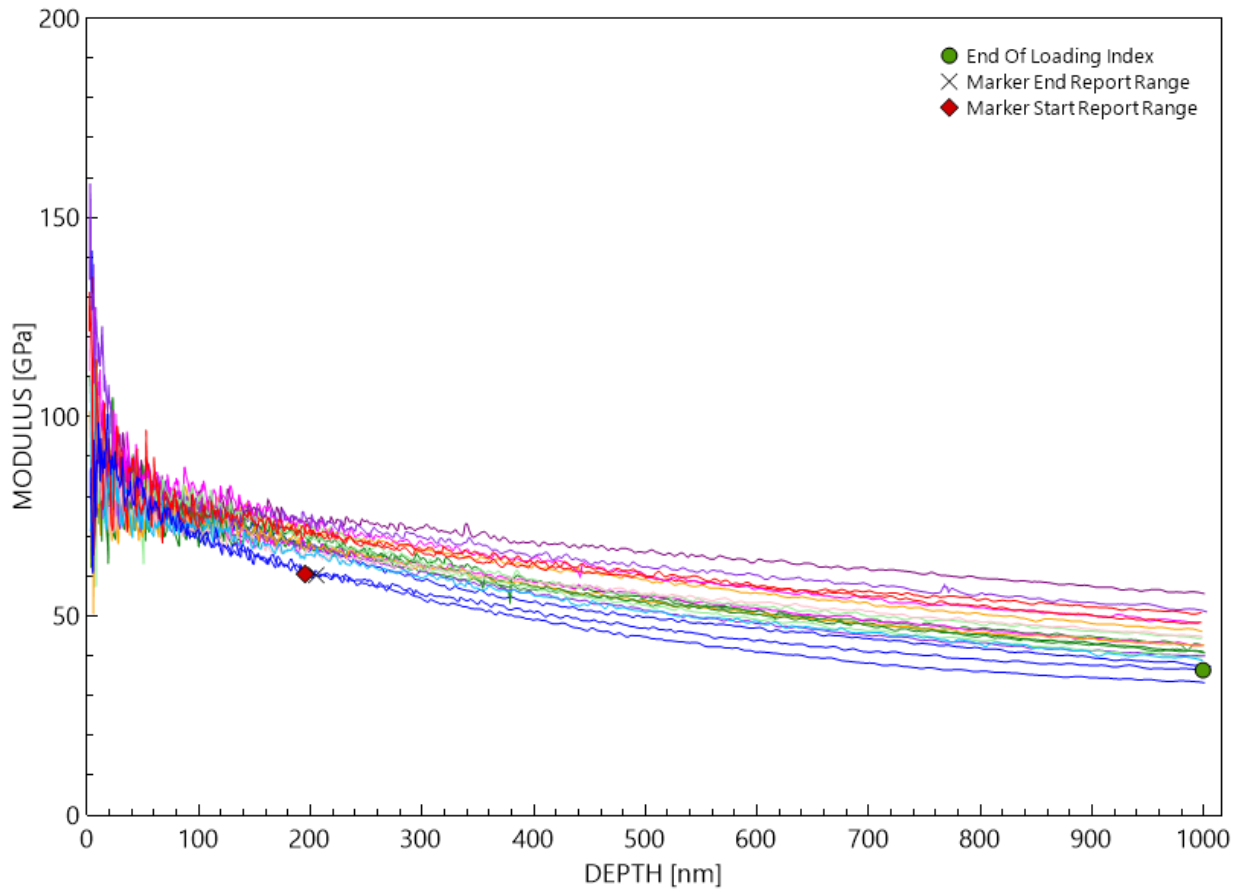


Figure 46: Modulus vs Depth data for AR-6061

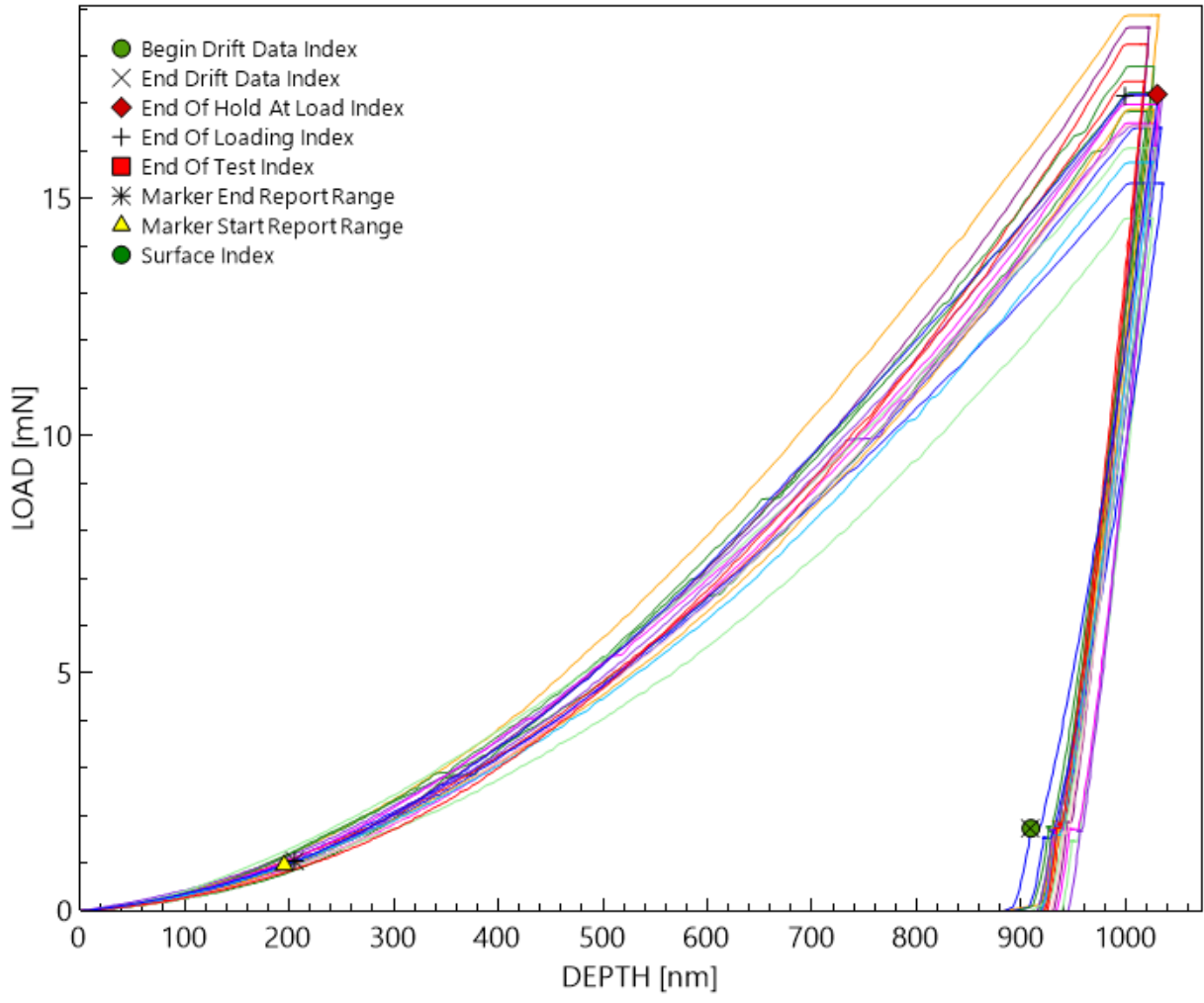


Figure 47: Load vs Depth data for AR-6061

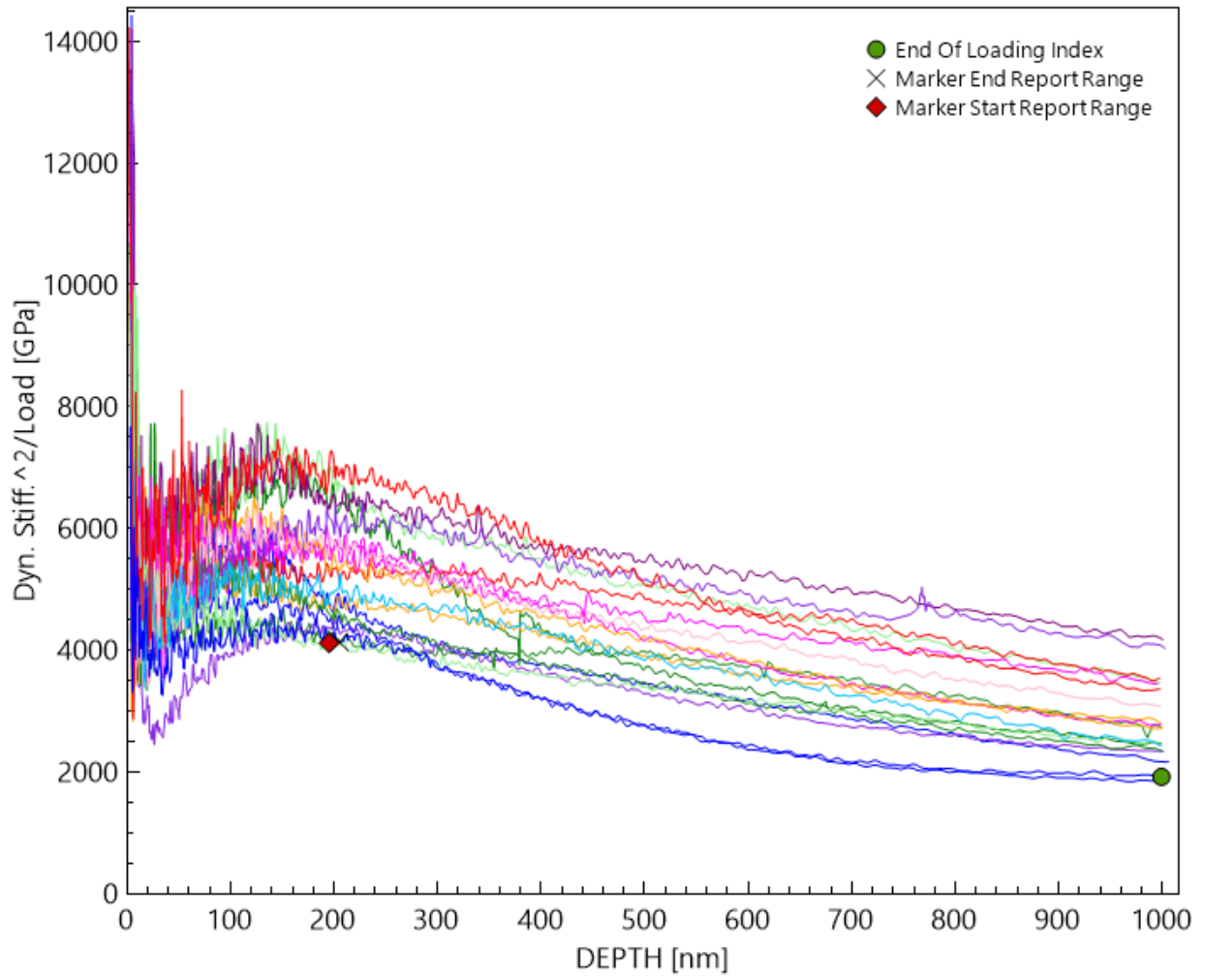


Figure 48: Dynamic Stiffness vs Depth data for AR-6061

11.3.2.Solutionized

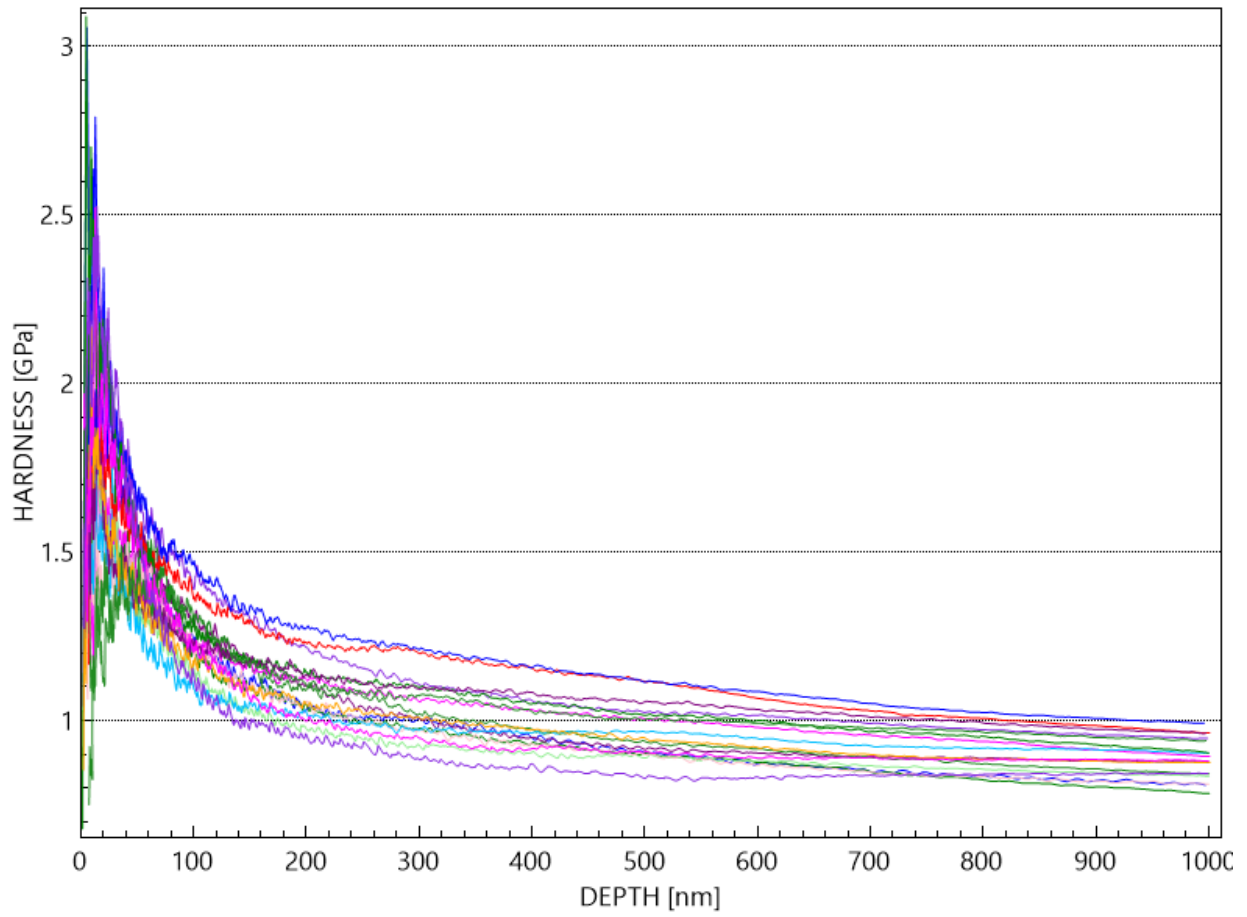


Figure 49: Hardness vs Depth data for Solutionized-6061

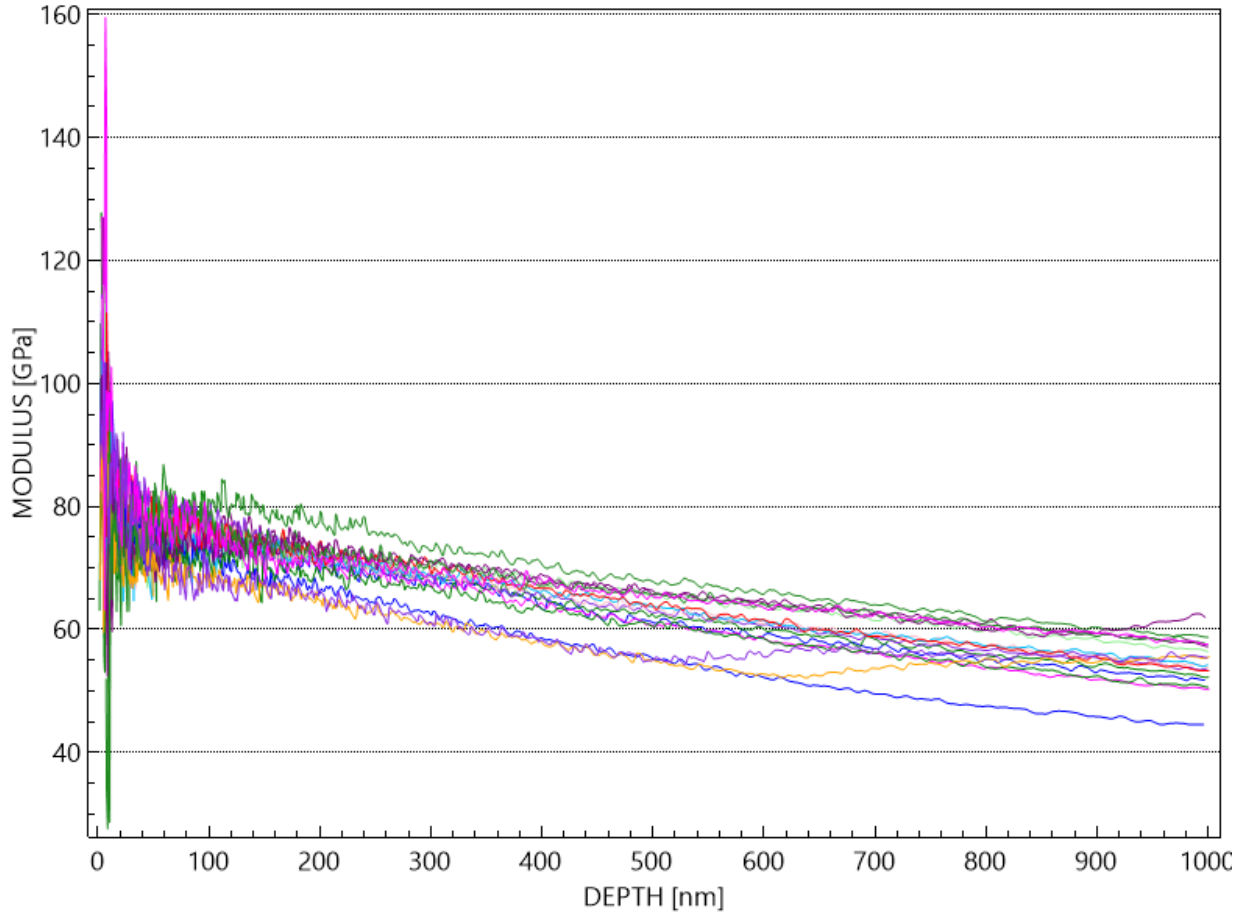


Figure 50: Modulus vs Depth data for Solutionized-6061

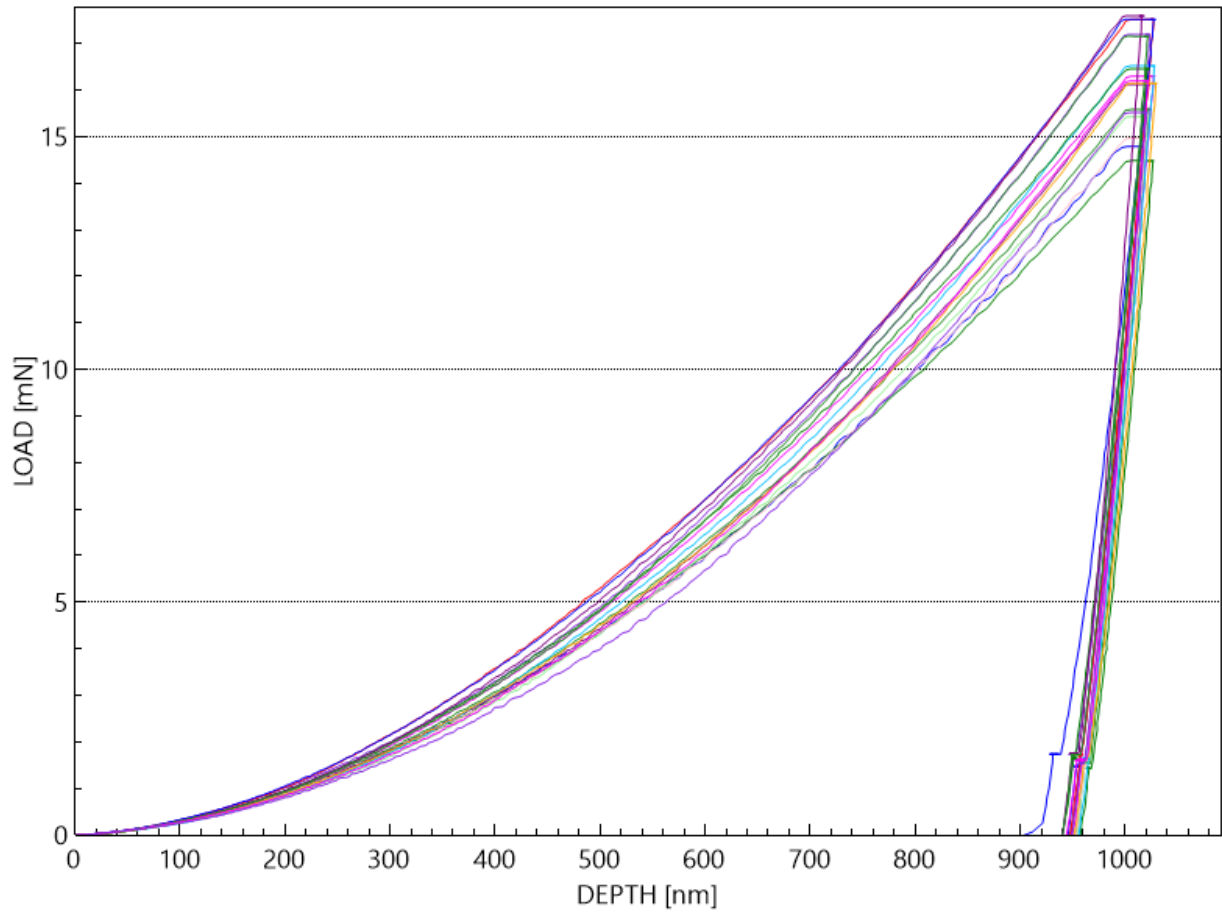


Figure 51: Load vs Depth data for Solutionized-6061